Sofia University
"St. Kliment Ohridski"

Master thesis of
Ralitsa Ivaylova Mancheva
Nuclear and Particle Physics, faculty No. 160380

Resonance laser ionization scheme development for Pb and Cd

Supervisor: Dr. Katerina Chrysalidis
Consultant: Prof. Dr. habil. Georgi Rainovski
September 27, 2023

Contents

1 Introduction

1.1 ISOLDE

The **I**sotope **S**eparator **O**n **L**ine **DE**vice (ISOLDE) is one of the oldest facilities at the European Organization for Nuclear Research (CERN). The facility produces a wide range of radioactive isotopes for a variety of different experiments in the realm of atomic and nuclear structure research, astrophysics, weak-interaction physics, solid-state physics and biomedical studies.

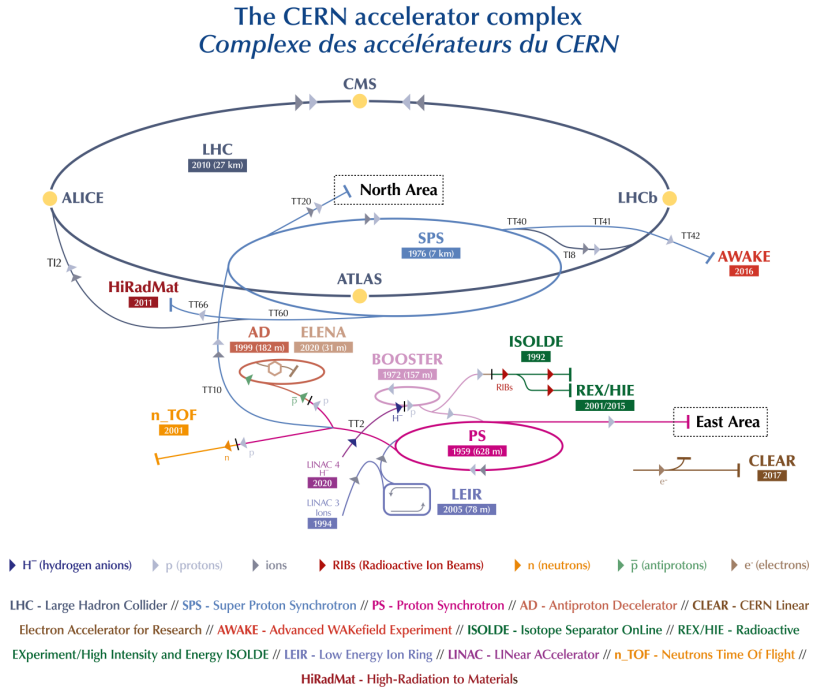

Figure 1.1: A schematic of the CERN complex with the ISOLDE facility on the right of the Proton Synchrotron Booster (lower right). Image taken from [1].

A proton beam from the Proton Synchrotron Booster (PSB) with an energy of 1.4 GeV impinges on a thick, heated target where fragmentation, spallation and fission interactions occur. The products are released into a resistively heated metal cavity, in which they can be ionised either via surface or resonance laser ionisation mechanisms. In a third approach, the products are released into a plasma ion source, where they are ionised via electron impact. The ions are then extracted via an electric field with between 30 to 60 kV and guided through one of the two mass separators (General Purpose Separator "GPS" or High Resolution Separator "HRS") for isotope selectivity. The resulting radioactive ion beam is then transported to a specific experimental setup through one of the several beamlines in the facility. ISOLDE produces a large variety of species with more than 1000 isotopes of 74 elements. The high purity and intensity of the radioactive beams makes ISOLDE a leading research facility.

The target material (most commonly uranium carbide) and the ion source are chosen depending on the isotopes that have to be produced. This thesis will focus on the **R**esonance **I**onization **L**aser **I**on **S**ource (RILIS) which provides element selective ionization for most of the ISOLDE experimental runs.

1.2 RILIS

The RILIS laser lab is an isolated laser protected area located in the ISOLDE hall and is situated over the so-called switchyard, where the beamlines from the two separators merge. It is one-of-a-kind, because it uses both solid state and dye lasers for resonant laser ionization (detailed summary in chapter 2) making it one of the most efficient and versatile laser ion sources worldwide. The spectral range covered with both types of lasers ranges from about 210 nm to 950 nm.

The RILIS setup consists of three to four tunable solid state Titanium:Sapphire (Ti:Sa) lasers designed by the LARISSA group in Mainz, Germany and three tunable dye lasers - two from Lioptec (model: Liopstar) and one from Sirah Lasertechnik GmbH (model: CREDO). All of these lasers are pumped by frequency doubled Nd:YAG lasers with a wavelength of 532 nm and a 10 kHz repetition rate. In addition to those, a Coherent/Lumera Blaze laser (Nd:YVO_4 at 532 nm) is used for non-resonant ionization into the continuum. In order to synchronise the timing of the laser pulses, which is crucial for the stepwise excitation of the atoms, all of the pump lasers can be externally triggered by a Quantum Composers 9530 pulse generator. Depending on the setup, there may be two lasers pumped by the same laser. In that case, delay lines may be necessary to provide adequate timing overlap.

There are two laser beam launch areas, leading down to the GPS and

the HRS frontends with path lengths of around 18 m and 23 m, respectively. Midway to the separator areas on the beam paths there are wedged fused silica plates at approximately normal incidence which reflect around 4 % of the laser beam power back into the laser lab. These reference beams are monitored by cameras and a Position Sensitive Device (PSD) as a diagnostics system for the laser beams going down into the ion source as it is not accessible during operations due to the high levels of radiation.

Also located in the reference area is the Photo-Ionization Spectroscopy Apparatus (PISA) where new schemes can be tested during the off-line period (see section 3.3). This apparatus was used for the majority of the testing done for the developments presented in this work.

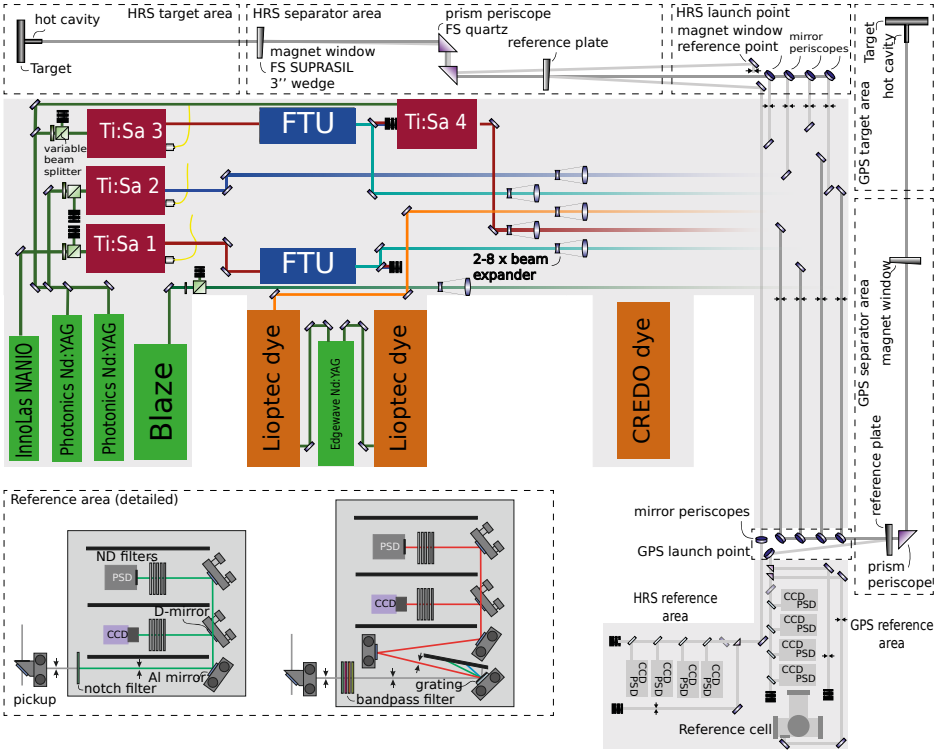

Figure 1.2: Layout of the RILIS setup. Green-coded lasers indicate pump lasers, orange-coded lasers indicate dye lasers and red-coded lasers indicate Ti:Sa lasers. Frequency-trippling units are shown in blue (FTU). Original image from [43] with modifications from Bianca Reich and additional modifications by Ralitsa Mancheva.

During the on-line period when ISOLDE is supplied with a proton beam, a typical RILIS run consists of setting up the lasers and optimizing them on wavelength and power. Afterwards, an optical beam path is set up to

launch the beam through the separator magnet and into the ion source. The observation system for the laser beam diagnostics is set up and after the laser beam has been launched and an ion signal has been established, the laser beams are once more optimized on the position, timing and overlap by observation of the ion signal. Then, the operations are handed over to the ISOLDE operators and for the length of the run the RILIS team is in on-call mode for maintenance and troubleshooting. The whole process can take anything from one up to five days, depending on the element that is being ionized and how different the required laser wavelengths are compared to the previous run.

1.3 Motivation

During the off-line periods, the main focus of RILIS is development of new, more efficient laser ionization schemes as well as other laser and ion source developments such as e.g. a Raman laser for increased wavelength coverage and linewidth reduction for high resolution applications [31–33], Time of flight laser ion source (ToF LIS), Laser Ion Source and Trap (LIST) [34], two-photon ionization [35], RILIS control system upgrades etc.

The focus of this thesis is on laser ionization scheme development for Pb and Cd. Since RILIS provides up to 65% of the ISOLDE beams, the time frame in which the switching between schemes happens is often very small. Keeping that in mind, scheme development is important not only for increasing the ionization efficiency of the elements, but also for simplifying as best as possible (without compromising the efficiency) the schemes in order to be able to switch between them easily and with minimal interventions required during the runs.

RILIS is the only laser ion source currently that uses both Ti:Sa and dye lasers. While that provides a very good coverage of the spectral range, a recurring problem with the generation of stable UV has been observed. Generation of UV beams with low wavelength and high power leads to a gradual power drop of the UV beam and visible white deposits on the UV optics. The problem was looked into in depth and was resolved (see section 3.4). Since most of the RILIS ionization schemes use a UV step, it was important to test the solution for stable UV generation with a typical laser ionization scheme, utilizing a UV-step. This serves as additional motivation for the scheme development of lead and cadmium since they both use a UV first step.

The scheme for lead, which has been in use until 2021, has three steps. It requires a dye laser and frequency tripled Ti:Sa and has an efficiency below 5%. It was proposed that the low efficiency might stem from population losses into dark states. This possibility was investigated, a different first step transition was tested and a new, more efficient scheme was developed

(see section 4.1).

The current laser ionization scheme for cadmium has three steps which use a frequency quadrupled Ti:Sa laser, a dye laser and a 532 nm step for non-resonant ionization. The main motivation for a new cadmium scheme is that the literature on cadmium is quite old [4] and it is possible to scan for a new second step that has not yet been listed that might yield a higher ionization efficiency. Furthermore, this would also give a possibility to replace a dye step with a Ti:Sa step. A detailed discussion can be found in section 4.2.

2 | Theoretical considerations

This chapter will summarize the underlying theory required for the understanding of the developments and concepts presented in this thesis. The chapter has been based on [21, 22].

2.1 Atomic structure

Hydrogen atom

Describing the atom in the context of quantum mechanics is quite difficult analytically since any many-body problem makes the calculations exceedingly difficult and long and in most cases unrealistic without numerical methods. The easiest atom to describe is naturally the hydrogen atom. From solving the time independent Schrodinger equation, we know that the electron can only have discrete energy levels in the Coulomb potential of the proton. The Schrodinger equation yields

$$H\left|\Psi\right\rangle = E\left|\Psi\right\rangle. \tag{2.1}$$

When expanding the Hamiltonian H to describe the kinetic energies of the proton and electron and the Coulomb potential, one obtains

$$-\frac{\hbar^2}{2m_e}\Delta_e\psi - \frac{\hbar^2}{2m_p}\Delta_p\psi - \frac{Ze^2}{4\pi\epsilon_0 r}\psi = E\psi(r_e, r_p) \tag{2.2}$$

where m_e and m_p are the masses of the electron and proton respectively, $q = Ze$ is the charge, $r_{e,p}$ are the radius vectors of the electron and proton and $\Delta_{e,p}$ are the Laplace operators with respect to $r_{e,p}$. If a spherically symmetric potential is considered, then it is more convenient to solve the equation in polar coordinates (r, θ, ϕ)

$$\frac{1}{r^2}\left[\frac{\partial}{\partial r}\left(r^2\frac{\partial}{\partial r}\right) + \frac{1}{\sin\theta}\frac{\partial}{\partial\theta}\left(\sin\theta\frac{\partial}{\partial\theta}\right) + \frac{1}{\sin^2\theta}\frac{\partial^2}{\partial\phi^2}\right]\Psi(r,\theta,\phi) = -\frac{2\mu}{\hbar^2}\left(E - V_C(r)\right)\Psi(r,\theta,\phi) \tag{2.3}$$

where $\mu = \frac{m_e m_p}{m_e + mp}$ is the reduced mass of the system and $V_C(r) = -\frac{e^2}{4\pi\epsilon_0 r}$ is the Coulomb potential.

Due to the spherical symmetry of the potential, the wave function can be expressed in terms of a radial part R_{ln} and an angular part Y_{lm}:

$$\Psi_{nlm}(r, \theta, \phi) = R_{ln}(r) Y_{lm}(\theta, \phi) \tag{2.4}$$

where $n \in \mathbb{N}$ is the principal quantum number, l is the orbital angular momentum ($0 \leq l < n$) and m is the magnetic quantum number ($-l < m < l$). l and m can have different values for the same n, but still lead to the same energy corresponding to a n^2 energy level degeneracy. The spherical harmonics $Y_{lm}(\theta, \phi)$ can be solved through the associated Legendre polynomials. Substituting R_{ln} with $u_n(r)/r$, one obtains

$$\frac{d^2 u_n(r)}{dr^2} + \frac{2\mu}{\hbar^2}\left[E_n + \frac{e^2}{4\pi\epsilon_0 r} - \frac{\hbar^2 l(l+1)}{2\mu r^2}\right] u_n(r) = 0. \tag{2.5}$$

From where one gains the eigenvalues for $u_n(r)$

$$E_n = -\frac{2\mu e^2}{\hbar^2 (4\pi\epsilon_0)^2 n^2} = -\frac{\mu e^2}{8\epsilon_0^2 h^2 n^2} = -R_\mu \frac{1}{n^2} \tag{2.6}$$

where R_μ is the mass-corrected Rydberg constant and μ is the reduced mass of the system. If the ground state of the atom is defined as the zero of the potential energy, then the ionizaion potential is defined as the convergence of the states of increasing principal quantum as $n \to \infty$, so that

$$E_{IP} = E_n + \frac{R_\mu}{n^2}. \tag{2.7}$$

Fine structure

The coupling of of electron spin and orbital momentum as well as relativistic effects lead to the removal of energy level degeneracies for the same n otherwise known as fine structure splitting (FS - splitting). This can be derived from additional terms in the Hamiltonian that accounts for these additional effects on the atom and can be solved using perturbation theory:

$$H = H_0 + H_{rel} + H_{ls} + H_D. \tag{2.8}$$

H_{rel} is the relativistic term accounting for that effect on the electron in the proton Coulomb potential. Taking into account the energy-momentum relation for the electron $E = \sqrt{p_e^2 c^2 + m_e^2 c^4}$ (with p_e being the momentum of the electron, m_e - the mass of the electron and c - the speed of light), one can see that the electron gains in mass and therefore in kinetic energy. H_D is the so-called Darwin term. It accounts for the uncertainty in the electron

position with precision higher than $\lambda_{compton} = \hbar/(m_e c)$ and only affects the s-orbit changing the effective potential of the nucleus. H_{ls} accounts for the coupling of the spin s of the electron with its orbital angular momentum l giving a full angular momentum $\mathbf{j} = \mathbf{l} + \mathbf{s}$ where the ($|l - s| \leq j \leq l + s$):

$$\Delta E \approx \frac{\mu_0 Z e^2}{4\pi m_e^2 r^3}(\mathbf{l} \cdot \mathbf{s}) \propto \frac{\hbar^2}{2}[j(j+1) - l(l+1) - s(s+1)]. \tag{2.9}$$

After further calculations taking into account the probability of finding the electron at position r and the hydrogen wave functions, for the total energy one gets:

$$E_{nj} = E_n \left[1 + \frac{Z^2\alpha^2}{n}\left(\frac{1}{j+1/2} - \frac{3}{4n}\right)\right] \tag{2.10}$$

where $\alpha = \frac{e^2}{4\pi\epsilon_0\hbar c} \approx \frac{1}{137}$.

Hyperfine structure

The hyperfine structure observed due to nucleus-electron interactions arising from nuclear structure effects is characteristic to different nuclei. The nucleus with spin I has a magnetic moment μ_K that interacts with the electronic magnetic field B_j. This leads to a $(2F + 1)$ component hyperfine splitting where $F = I + j$ is the total angular momentum. The additional hyperfine structure energy is thus

$$\Delta E_{HFS} = \frac{A}{2}[F(F+1) - j(j+1) - I(I+1)] \tag{2.11}$$

where $A = g_N \mu_K B_j / \sqrt{j(j+1)}$ is the hyperfine structure constant and g_N is the nuclear g-factor. From this, one can obtain the selection rule $|I - J| \leq F \leq I + J$ where a transition is only possible if ΔF is ± 1 or 0. The hyperfine structure splitting it typically several orders of magnitude smaller than the fine structure splitting.

2.2 Light interacting with matter

In order to clearly explain the RILIS principle and in general to discuss lasers, it is useful to first touch on the physical processes behind light-matter interaction. The energy conservation law yields three possibilities of photon-atom interaction for a two-level system with initial state $|1\rangle$ and final state $|2\rangle$ with energies $E_1 < E_2$:

- **Absorption**: The atom absorbs a photon with energy $h\nu$ to transition from $|1\rangle$ to $|2\rangle$ with the new energy of the electron expressed as $E_2 = E_1 + h\nu$.

- **Spontaneous emission**: An electron spontaneously transitions from $|2\rangle$ to $|1\rangle$ by emission of a photon with energy $h\nu = E_2 - E_1$ in an arbitrary direction.
- **Stimulated emission**: A photon from an external field with energy $h\nu$ stimulates the emission of another photon with the same energy and direction of propagation with the electron going from $|2\rangle$ to $|1\rangle$.

The probabilities for these transitions are described by the Einstein coefficients A_{21} for spontaneous emission and B_{21} for stimulated emission. Due to the energy conservation, the absorption must be equal to the total emission, therefore

$$B_{12}\omega_\nu N_1 = (B_{21}\omega_\nu + A_{21})N_2 \tag{2.12}$$

where ω_ν is the radiation field and $N_{1,2}$ are the number densities.

Assuming a thermal equilibrium, the ratio N_2/N_1 follows the Boltzmann distribution

$$\frac{N_2}{N_1} = \frac{g_2}{g_1} e^{(E_1 - E_2)/(kT)} = \frac{g_2}{g_1} e^{(h\nu)/(kT)} \tag{2.13}$$

where $g_{1,2}$ is the statistical weight of a state with energy $E_{1,2}$ and total angular momentum quantum number J. If the Planck formula for the spectral energy density of the thermal radiation field is applied

$$\omega_\nu = \frac{8\pi h\nu^3}{c^3} \frac{1}{e^{(h\nu)/(kT)} - 1} \tag{2.14}$$

and inserting Equation 2.13 into 2.12, one obtains

$$B_{21} = \frac{g_1}{g_2} B_{12} \tag{2.15}$$

and

$$A_{21} = \frac{8\pi h\nu^3}{c^3} B_{21}. \tag{2.16}$$

The wave functions $\psi_{1,2}$ of the initial and final states have to be taken into account for a transition from E_2 to E_1. The transition dipole moment (also known as Matrix element) M_{21} is thus defined as

$$M_{21} = e \int \psi_2^* r \psi_1 d\tau. \tag{2.17}$$

If a Matrix element has a value zero, this transition is forbidden which therefore implies selection rules for allowed transitions:

$$\begin{gathered} \Delta J = 0, \pm 1 \quad \text{where} \quad J = 0 \to 0 \quad \text{is forbidden} \\ \Delta m_J = 0, \pm 1 \quad \text{where} \quad m_J = 0 \to 0 \quad \text{is forbidden if} \quad \Delta J = 0 \end{gathered} \tag{2.18}$$

For LS coupling $\Delta S = 0$, $\Delta L = 0, \pm 1$ and $\Delta l = \pm 1$ (for the electron transitioning) apply. In jj coupling, $\Delta j = 0, \pm 1$ for one electron and $\Delta j = 0$ for the rest of the electrons. The parity of the final state in regards to the initial state has to change as a photon (negative parity) is absorbed, so $\pi_i = -\pi_f$.

2.3 Lasers

As the abbreviation suggests, the laser (Light Amplification by Stimulated Emission of Radiation) is a coherent, monochromatic source of light based on stimulated emission (see section 2.2). The source of external energy necessary to start this process can be of various different types, but very commonly it is another laser (so-called 'pump laser'). In order to ensure a constant cycle of excitation and emission over time, the requirement for a lasing medium is to have a higher number of electrons in an excited state than the number of electrons in a lower energy state. This process is the so-called 'population inversion'. The gain medium is thus chosen with specific shape, size, purity, concentration (etc.) that provide the optimal conditions for maximum lasing efficiency. The gain medium can be gas, liquid, solid or plasma. However, it is also necessary for the light to oscillate back through the gain medium which is achieved through a set of two mirrors that form the 'resonator' of the laser in order to achieve amplification through stimulated emission. One of the mirrors is a high-reflective mirror that reflects almost all of the light back through the medium. The opposite mirror is an output coupler that reflects some of the light back into the gain medium (enough to keep the amplification process going) and transmits the rest of it out to form the laser beam. The output beam can be continuous or pulsed with fixed wavelength or tunable and there are many varieties of lasers depending on their gain medium. For the purposes of this work, only tunable pulsed titanium-sapphire lasers will be discussed with a brief mention of tunable pulsed dye lasers. The resonator, as well as the pump laser optics and any other elements added to the system are all situated in a 'laser cavity' that can have different geometries, depending on the specific usecase.

2.3.1 Tunable lasers

This subsection is largely based on the book 'Laser Spectroscopy. Basic concepts and Instrumentation' by W. Demtroeder [21].

As previously mentioned, the RILIS lasers cover the spectral range between 210-950 nm. This requires lasers with tunable wavelengths and is achieved by using laser media with wide emission spectra and combining them with frequency-selective elements in the laser cavity. The most commonly used such elements are Lyot (or birefringence) filters, often used in

combination with an etalon, gratings, polarization dependent optical elements and wavelength selective optical coatings.

Among those wavelength-selective elements, the etalons, Lyot filter and grating fall under the general category of interferometers. The basic principle of all interferometers is as follows: The incident light on the interferometer is divided into two or more partial beams by internal reflections which leads to different optical path lengths before the beams are superimposed again at the exit of the interferometer. The total amplitude of the transmitted wave, which is a result of the interference between the partial waves, depends on the amplitudes A_k and the phases $\phi_k = \phi_0 + 2\pi s_k/\lambda$ of the partial waves (where s_k are the optical path lengths of the partial waves). Therefore, the amplitude of the resulting wave is dependent on the wavelength λ and the maximum intensity is achieved when all the partial waves interfere constructively. Thus, the condition for the differences in optical paths $\Delta s_{ik} = s_i - s_k$ is

$$\Delta s_{ik} = m\lambda, \quad m = 1, 2, 3... \tag{2.19}$$

This condition applies for all wavelengths for which

$$\lambda_m = \Delta s/m, \quad m = 1, 2, 3... \tag{2.20}$$

The wavelength interval is thus

$$\delta\lambda = \lambda_m - \lambda_{m+1} = \frac{\Delta s}{m} = \frac{\Delta s}{m+1} = \frac{2\lambda}{2m+1} \tag{2.21}$$

where $\lambda = \frac{1}{2}(\lambda_m + \lambda_{m+1})$ is called the 'free spectral range' (FSR) of the interferometer. This can be rewritten in terms of the free spectral frequency range as

$$\delta\nu = \nu_{m+1} - \nu_m = c/\Delta s \tag{2.22}$$

which is independent of the order m.

Lyot filter

A Lyot (or birefringence) filter (named after its inventor B. Lyot [23]) is an interferometer which uses 2 partial waves with mutually orthogonal polarization. It works as a narrow passband optical filter of transmitted wavelengths that is based on the physical process known as birefringence.

Any optically transparent material in which the refractive index depends on the polarization direction of the incident light is "birefringent". Such materials include crystalline quartz, calcite, sapphire, ruby and non-linear crystals like $LiNbO_3$, LBO etc. Birefringence can only occur in optically non-isotropic materials through intrinsic anisotropy or it can be induced

in some cases by mechanical stress, strong electric fields or through design asymmetries (for example in an optical fiber).

A Lyot filter consists of a sequence of alternating polarizers and birefringent plates with each plate having a different thickness to the previous one by some integer ratio (in the case of the Ti:Sa cavities used at RILIS, the ratio of thickness is $1 : 4 : 16$). In its simplest configuration, each crystal is oriented at 45 deg to the axis direction of the polarizers with the beam perpendicular to the plates (see Figure 2.1).

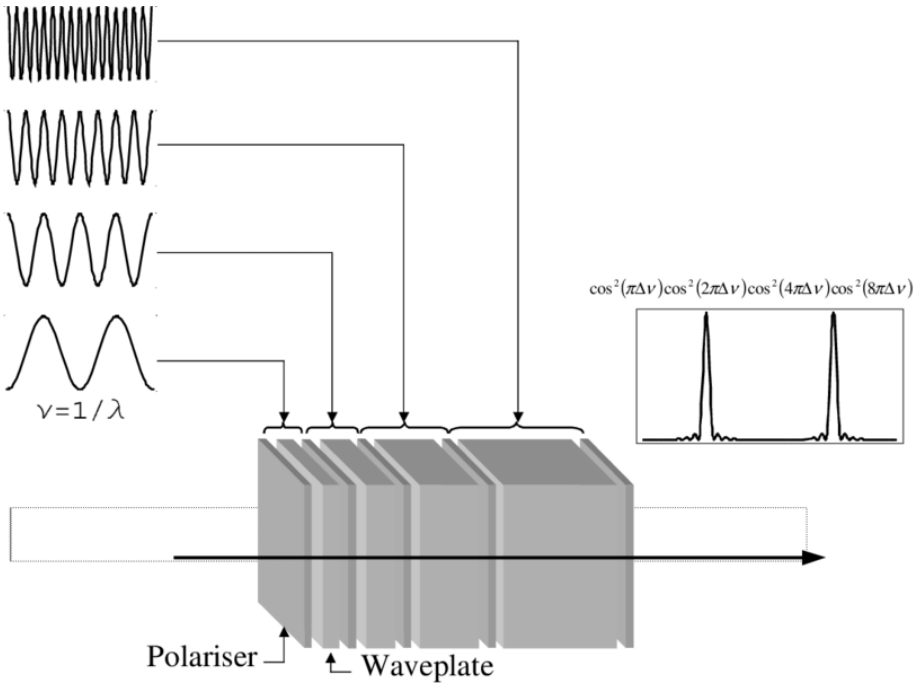

Figure 2.1: A schematic showing a Lyot filter with four birefringent plates with polarizers between them with increasing width. The transmission modes can be seen on the diagram on the right [24].

By rotating the filter, the polarization of the light is changed and thus the refractive index changes as well. Consequently the wavelength can be chosen depending on the rotation angle, since the polarization dependent elements inside the cavity reflect out all frequencies with non-optimal polarization.

The birefringent crystal has different refractive indices n_o and n_e for the ordinary and extraordinary waves. The ordinary wave is polarized in the x-y-plane perpendicular to the optical axis, whereas the extraordinary wave has its electrical field vector in a plane defined by the optical axis and the incident beam [21]. This leads to an elliptical polarization of the transmitted beam with a phase shift of

$$\delta\lambda = \frac{2\pi}{\lambda}(n_o - n_e)L \tag{2.23}$$

with L being the length of the crystal. Since the light amplification inside the Ti:Sa crystal is polarization-dependent and since the Ti:Sa crystal is cut at a Brewster angle, a strong loss of the s-polarized light component is achieved and so only p-polarized light is significantly amplified. If one assumes parallel polarization of the incident and transmitted p-polarized light, the transmission function is then

$$I(\lambda) = I_0 cos^2\left(\frac{(n_o - n_e)\pi L}{\lambda}\right). \tag{2.24}$$

The free spectral range of a Lyot filter is given by

$$\delta\nu = \frac{c}{L(n_o - n_e)}. \tag{2.25}$$

Etalon

An etalon, also known as a Fabry-Perot interferometer (FPI) is a multiple-wave interferometer that can be used for fine adjustment of the wavelength selection and laser linewidth in a laser cavity. It consists of two parallel partially reflective plates with the inner surfaces (facing each other) coated with a reflective coating and the outer surfaces (facing outwards) coated with anti-reflection coatings.

If the incident beam is passing through an etalon with distance between the plates d and the light propagation medium has a refractive index n, then for an angle β relative to the planar surface, the wavelength for the transmission maximum of mth order is

$$\lambda_m = \frac{2d}{m}\sqrt{n^2 - \sin^2\alpha} = \frac{2nd}{m}\cos\beta. \tag{2.26}$$

For all wavelengths $\lambda = \lambda_m$ (m=0,1,2,...) in the incident light, the phase difference between the transmitted partial waves becomes

$$\delta = 2m\pi = \frac{2\pi}{\lambda}2nd\cos\beta. \tag{2.27}$$

If the reflectivity of the FPI surfaces is R, then the transmission function, defined by an Airy function, is

$$I(\beta) = I_0\frac{(1-R)^2}{(1-R)^2 + 4R\sin^2(\beta/2)}. \tag{2.28}$$

Defining $q = 4R/(1-R)^2$, one can obtain the so-called 'finesse' F^* of the etalon

$$F^* \sim \frac{\pi\sqrt{q}}{2} \tag{2.29}$$

which is a measure for the effective number of interfering partial waves in the interferometer and is the ratio between the full width at half maximum (FWHM) of the transmission peaks and the free spectral range.

Grating

A grating interferometer can be placed inside of a laser cavity as a frequency selective element. The grating is a reflective surface that consists of many (in the order of 10^5) straight grooves parallel to the entrance slit of the box it is placed in. The light from the grating is focused onto a spherical mirror onto the exit slit. The incident light diffracts from each groove (where the groove width is $d \approx \lambda$) into a large range $\Delta r \approx \lambda/d$ of angles r around the direction of geometrical reflection (see Figure 2.2). The total reflected light is a coherent superposition between the micro reflections from the grating grooves. Only in the directions where these reflection waves are in phase will constructive interference contribute to a large total intensity. All other reflections will interfere destructively. The path difference of two parallel beams onto two adjacent grooves at an angle α (shown in Figure 2.2 (b)) is $\Delta s = \Delta s_1 - \Delta s_2$. Since there is constructive interference in the direction β of the two beams, Δs is an integer multiple m of the wavelength λ and thus one obtains the grating equation

$$d(\sin\alpha \pm \sin\beta) = m\lambda. \tag{2.30}$$

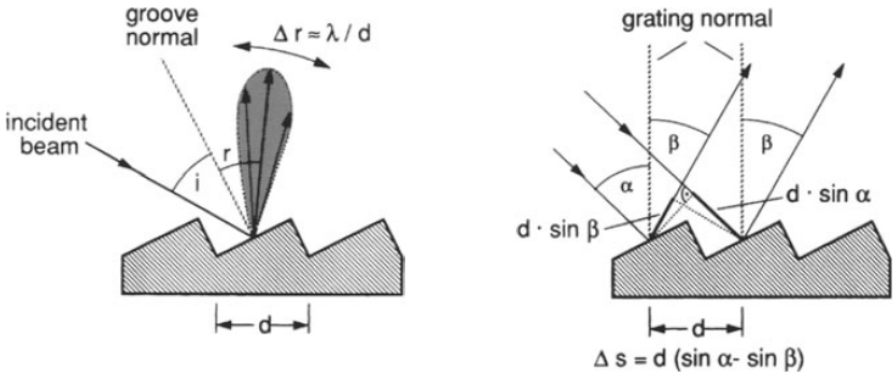

Figure 2.2: (a) Reflection of incident light from one groove into the diffraction angle λ/d. (b) Illustration of the grating equation 2.30. Figure taken from [21].

2.3.2 Harmonic generation

Harmonic generation refers to a nonlinear optical effect in which n photons interact with a nonlinear optical medium and as a result, the photons are 'combined' to generate a new photon with n-times the frequency of the incident photons (and thus a wavelength divided by n). At RILIS the orders $n = 2, 3, 4$ (referred to as second, third and fourth harmonic generation) are used in order to respectively double, triple and quadruple the fundamental frequency of the Ti:Sa lasers.

Waves propagating inside a nonlinear medium induce nonlinear polarization. This acts as a source of new waves at frequencies $\omega = \omega_1 \pm \omega_2$, which propagate through the medium with phase velocity $v_{ph} = \omega/k = c/n(\omega)$. The atoms in the medium produce microscopic waves. Since the atoms are in different positions, the microscopic waves can have a macroscopic effect with a non-negligible amplitude only if the incident waves and the polarization waves are properly matched. If the atoms have locations r_i, then the phases of all their contributions $P_i(\omega_1 \pm \omega_2)$ must be equal at a given point within the pump beam. The amplitudes $E_i(\omega_1 \pm \omega_2)$ then add up in phase in the direction of the pump beam and the intensity increases with the length of the interaction zone. This is the so-called 'phase matching condition' and it can be written as

$$k(\omega_1 \pm \omega_2) = k(\omega_1) \pm k(\omega_2). \tag{2.31}$$

This may be interpreted as a conservation of momentum for the three photons participating in the mixing. For a specific wavelength, the phase matching can be achieved either by turning the crystal orientation against the beam orientation (angle tuning) or through temperature control (temperature tuning) [21, 25]. The choice of nonlinear medium depends on the wavelength of the laser beam and the tuning range. At RILIS BiBO and BBO crystals are used.

2.4 Laser ionization mechanisms

The RILIS method of ionization is based on a stepwise excitation of the valence electron in an atom with pulsed lasers tuned to match the energy of the consecutive atomic transitions. As the energy levels in the atoms are element specific, this allows to choose such excitation steps that are unique to a single element which provides the selectivity of ionization. There are different physical mechanisms through which the ionization potential (IP) of the atom can be reached and release the outer electron leaving an ionic (singly charged) core. The three ways this is achieved at RILIS are through a resonant auto-ionizing state, via a high-lying Rydberg state (with consecutive ionization e.g. through black-body radiation, field ionization or

absorption of another laser photon) or through non-resonant ionization into the continuum.

Non-resonant ionization

The most universal method of ionization is by supplying a photon with enough energy over an excited step to surpass the ionization potential energy

$$h\nu \geq E_{IP} - E_i \tag{2.32}$$

where E_i is the energy of the last intermediate state and E_{IP} is the ionization potential. This method is advantageous, because not every element possesses resonant states above the IP that are accessible with the RILIS lasers whereas practically any atom can be supplied with enough electromagnetic radiation energy to release an electron from the outer shell. The limitations of this mechanism are that the ionization efficiency is limited by the available amount of power for the non-resonant ionization step. Since it cannot be saturated, the ionization linearly depends on the available power, whereas a resonant state can often be saturated with low to moderate powers and oftentimes leads to higher overall efficiencies [17].

Ionization via a Rydberg state

Any atom can also be easily excited to a state with high principal quantum number n and high energy close to the IP threshold. Such states grow denser when going closer to the IP and ultimately converge to this limit

$$\lim_{n\to\infty} E_n = IP. \tag{2.33}$$

Since the energy necessary to get from a Rydberg state to the IP is low, a Rydberg atom can be ionized through an external electric field, blackbody radiation, through collisions or even a second photon with the same energy as one of the previous excitation steps. The outer highly excited electron experiences a screening effect from the nucleus with charge Z by the Z-1 other electrons. This occurrence is analogous to the hydrogen atom, hence the name 'Rydberg atom'. The energy is dependent on the principal quantum number n and can be written as follows:

$$E_n = E_{IP} - \frac{R_\mu}{(n^*)^2} = E_{IP} - \frac{R_\mu}{(n - \delta(n))^2} \tag{2.34}$$

where $\delta(n)$ is the so-called quantum defect, E_{IP} is the ionization potential, R_μ is the mass-corrected Rydberg constant and n^* is the effective principal quantum number which is introduced to correct for the common case of non-hydrogen atoms.

The quantum defect $\delta(n)$ is a measure of the screening of the outer electron from the nucleus by the other electrons. Its dependency on n can be

neglected for large n. For small n, the Ritz series expansion of the quantum defect is sufficient:

$$\delta(n) = \delta_0 + \frac{a}{(n-\delta_0)} + \frac{b}{(n-\delta_0)^2} + \mathcal{O}(n^6) \tag{2.35}$$

Therefore, for the energy dependence on the principal quantum number one obtains

$$E_n = E_{IP} - \frac{R_\mu}{(n-\delta(n))^2} \approx E_{IP} - \frac{R_\mu}{[n-\delta_0 - \frac{a}{(n-\delta_0)}]^2}. \tag{2.36}$$

Resonant ionization via an auto-ionizing state

The most efficient mechanism of ionization is through a so-called auto-ionizing state. This refers to bound states over the IP which are the result of two or more excited electron interactions. These electrons transition to discrete states which affect the overall excitation energy of the atom. Once this energy exceeds the ionization threshold, it can be rapidly redistributed among the excited electrons non-radiatively which leads to the emission of a free electron. These are typically the states that are searched for when developing a new ionization scheme.

An illustrative, simplified overview of these three mechanisms can be seen in Figure 2.3.

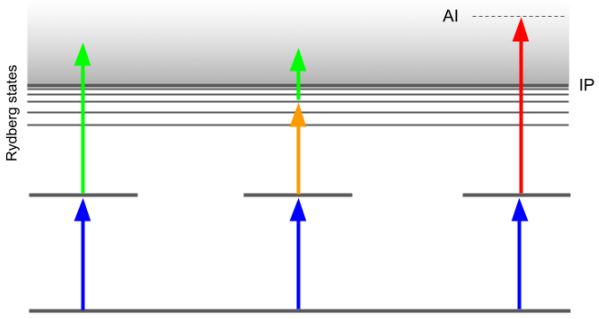

Figure 2.3: Schematic showing the three mechanisms used for ionization at RILIS. Left: non-resonant ionizatioin into the continuum. Center: ionization via a Rydberg state (non-resonant given as example, but that does not exhaust the possibilites for the ionization mechanism). Right: ionization via an autio-ionizing state (AI) above the IP. For simplicity, the schemes are drawn with least possible number of steps.

3 | Experimental setup

3.1 RILIS laser system

3.1.1 Ti:Sa lasers

The design of the 10 kHz pulsed tunable Ti:Sa lasers that are used at RILIS was developed at the University of Mainz [26, 27] and is continuously evolving with new laser developments. The laser has a Z-cavity design (stemming from the shape that the resonator forms, see Figure 3.2) and the gain medium is a titanium doped sapphire crystal (Ti^{3+}:Al_2O_3) cut at Brewster angle.

The tuning range of the Ti:Sa crystal is roughly between 700 nm and 950 nm. However, the resonator has specific mirror sets that are coated for maximum reflectivity in the specific wavelength ranges (see Figure 3.1).

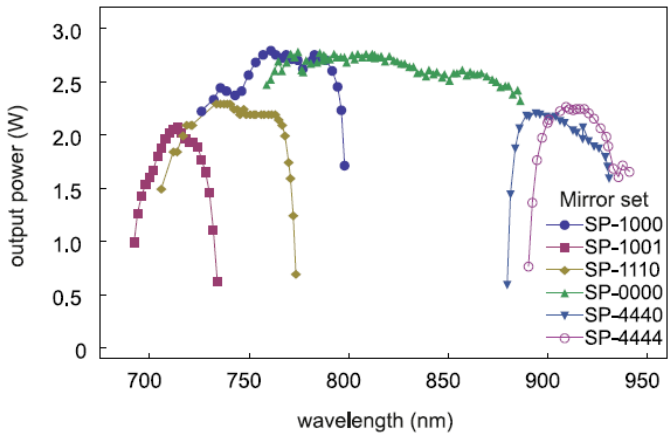

Figure 3.1: The tuning range of the Ti:Sa laser covered by different mirror sets (sets 0, 1 and 4 are most commonly used) with 10 W input power. The notation SP-EHHA refers to the combinations of different mirrors from these sets, where E is the end mirror, H are the curved mirrors and A is the output coupler. Image taken from [28].

Cavity elements

The optics are mounted on a base plate with a thickness of 30 mm and the beam height is chosen to be 25.4 mm (1 inch). The distance between the curved mirrors and the position of the crystal are fixed in order to minimize the degrees of freedom and to make the setting up of the laser as simple as possible. All of the mirrors are mounted onto mounts that have two adjustment knobs for the vertical and horizontal axis.

The cavity of the Ti:Sa consists of two mirrors that guide the pump beam into the cavity and a focusing lens then focuses the pump beam into the crystal. The crystal is placed between two curved mirrors that form the resonator of the laser along with the end mirror and the output coupler. A Fabry-Perot etalon is placed just in front of the end mirror and a Lyot filter is situated before the output coupler, close to the crystal. There are also slots for additional elements like a frequency doubling crystal or two mirrors (one on a magnetic mount) for the position adjustment of the alignment diode beam.

The grating Ti:Sa is set up in a very similar way with the end mirror replaced by a grating with a system of prisms (referred to as prism beam expander) just before the grating (see Figure 3.2).

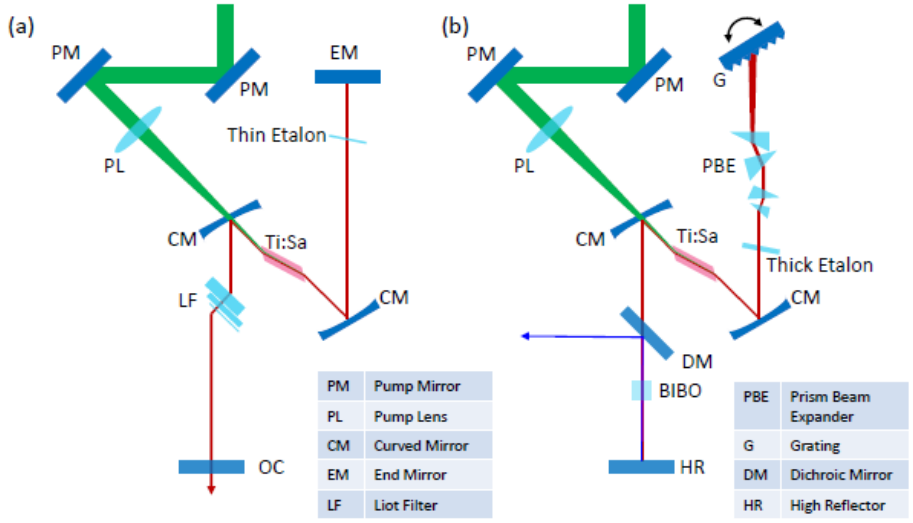

Figure 3.2: (a) Ti:Sa cavity used at RILIS. (b) Grating Ti:Sa with intra-cavity frequency doubling and linewidth narrowing by introducing a thick etalon. Image taken from [29].

Setting up of the cavity

The setting up of a Ti:Sa laser generally follows the same steps:

- **Prealignment:** Before the pump beam is let into the cavity, the cavity is prealigned using a diode laser, the light from which is entering on the opposite side of the cavity from where the pump beam enters. Alignment tools with small apertures are used in order to center the beam onto the curved mirrors.

- **Alignment:** The pump beam is let in the cavity and adjusted in position with the pump mirrors until the cavity lazes. The power is optimized on a powermeter by adjusting the output coupler, end mirror and one of the pump mirrors as well as by adjusting the pump beam focus with the lens.

- **Wavelength selection:** The Lyot filter and the etalon are installed and some of the output light is coupled to a wavemeter. With the birefringent filter, the wavelength is preselected and then fine tuned with the etalon. The alignment of the cavity is periodically optimized with the mirrors.

Frequency generation

Whenever frequency doubling of the Ti:Sa is necessary, it is usually done by mounting a frequency doubling crystal inside the cavity close to the end mirror. The cavity has to be closed - the end mirror is replaced with a high reflector mirror. The blue light from the doubling crystal is then coupled out using two mirrors - one that reflects the blue light and transmits the red and a high reflector.

If the frequency has to be quadroupled, the output blue light passes through another doubling crystal outside the cavity which is mounted on a rail with a focusing lens in front of it. The beam coming from the cavity is guided with two mirrors to the rail and is aligned so that it passes through the center of the lens and onto the crystal. It is important to be careful with the placement of the crystal in regards to the beam focus as the beam can damage the crystal if it is focused on its surface. The crystal can also be damaged if the beam is too focused so the lens has to be chosen accordingly. Once the beam is focused inside the crystal, the generated UV beam is separated from the blue with a Pellin Broca prism (see Figure 3.3). Once the angle of the crystal and the position of the focus are optimized on the UV power, the Pellin Broca prism is replaced with a UV-reflective mirror.

In order to triple the frequency, sum frequency mixing is used. When two photons with frequencies ω and 2ω pass through the nonlinear crystal, the output is one photon with frequency 3ω. In order for this process to be efficient, phase matching is necessary. The fundamental (so red/IR) output light of the Ti:Sa is coupled out to a tripling unit which consists of two non-linear crystals with corresponding lenses and optics coated specifically to transmit red and reflect blue and vice versa. All of these elements are

mounted on rails. After frequency doubling the fundamental light from the Ti:Sa cavity, the blue and red are split by a so-called dichroic mirror. Afterwards, the beams are aligned through lenses, specifically coated for the respective wavelength ranges (blue/red). Since the polarisation of the red and the blue is exactly orthogonal after the frequency doubling, the polarisation of the red light is turned by ninety degrees, so it matches the one of the blue. Another dichroic mirror is then used for overlapping the red and blue light inside the non-linear crystal for UV generation.

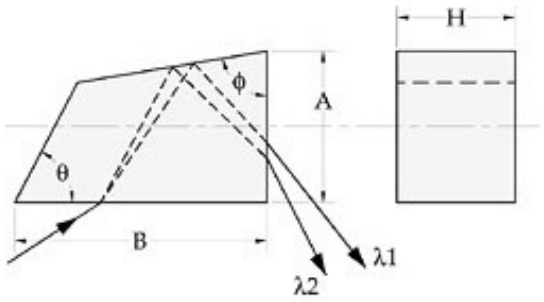

Figure 3.3: A Pellin Broca prism showing the incident beam being split into two beams with different wavelengths due to their different velocities inside the optical medium of the prism. Image taken from [30].

Beam path

After the necessary wavelength selection and frequency mixing is finished, the beam has to be transported to the ion source. In order to focus the beam into the source, an adjustable two-lens system is used. It consists of two lenses mounted on a rail which have to be prealigned so that the beam passes through the center of each. By adjusting the distance between them, the focal length can be changed. Afterwards the beam is sent down to the ion source with launch mirrors that are mounted on piezo mounts. Using these mounts enables fine adjustments of the optical beam path which is required as small changes in the angle of the crystal lead to big offsets of the beam due to the large distance to the source.

3.1.2 Dye lasers

The gain medium of dye lasers are highly-fluorescent organic dye molecules dissolved in an organic solvent (most commonly ethanol or DMSO). The different dyes have specific absorption and emission spectra with a typical tuning range of 20-50 nm. RILIS uses around 15 types of dye solutions (see section 3.4) that cover ranges of 540-860 nm (when pumped with 532 nm) and 390-580 nm (when pumped with 355 nm) at a repetition rate of 10 kHz [17].

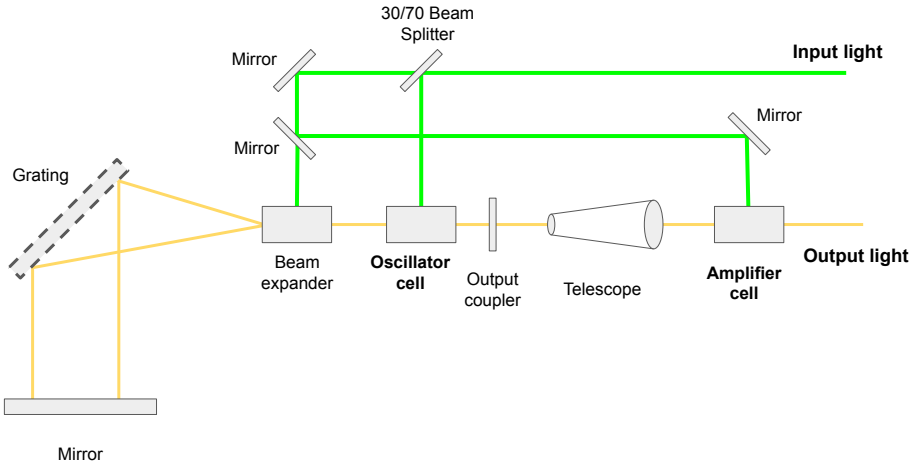

Figure 3.4: Schematic representation of a dye laser in the Littman-Metcalf configuration.

The input light coming from the 532 nm pump beam is split with a beam splitter mirror that transmits 30% of the light and reflects the rest. The oscillator cell is a thin cuvette through which the dye solution is pumped and acts as a gain medium for the laser. The light passing through the beam expander goes onto the grating where by adjusting the angle of the mirror, the wavelength is selected. This is known as the Littman-Metcalf configuration [37]. Alternatively, the Littrow configuration does not include a mirror for the grating, but the wavelength is selected by rotating the angle of the grating itself [38]. The dye lasers at RILIS use the Littman-Metclaf configuration. After the resonator wavelength is selected in the oscillator cell, this light then acts as a 'seed' of the so-called amplifier cell which enhances the power of the output light (see Figure 3.4). However, the gain of the lasing medium is high enough to produce sufficient power even for single-pass amplification. Another advantage of the dye lasers is that they can be pumped by higher powered lasers (up to ∼60 W) whereas the Ti:Sa lasers have a more limited input pump power because of the damage threshold of the Ti:Sa crystal (up to ∼20 W). Frequency conversion is also possible with dye lasers as is the case with the Ti:Sa lasers. Therefore, the frequency doubled dye laser range is also accessible for the RILIS. However, the dye performance decreases over time due to a gradual change of the pH-level and thus, it is more practical to use a Ti:Sa laser wherever possible (as long as ionization efficiency is not compromised).

One of the drawbacks of using dye lasers is that they require frequent interventions during operations as dye changes are commonly necessary due

to the dye degradation. Also depending on the solvent, these dye changes can lead to unstable UV generation (see section 3.4). In comparison, Ti:Sa lasers require minimal interventions during operations if the beam is stable.

3.2 Launch system and ion source

The launch of the laser beams into the ion source happens using a set of dielectric mirrors located near the exit ports of the RILIS room. The beams then travel down to the source where half way down they pass through a wedged fused silica plate. The plate reflects ∼4% of the total beam back into the laser room to the observation area where the beam shape and position is monitored through position sensitive devices (PSD) and CCD cameras.

The RILIS lasers perform resonant ionization inside a hot cavity - a refractory metal tube which has an internal diameter $d = 3\,\text{mm}$ and length $L = 34\,\text{mm}$ that is resistively heated to typically ∼2000 °C. The target where the atoms are produced is connected to the cavity and once ionized, the ions are guided by an electric potential to the extraction aperture. The laser beams are directed along the length of the cavity (see Figure 3.5). Atoms that have a low ionization potential (less than 6 MeV) can be easily ionized thermally in the hot cavity environment which causes isobaric contamination. This effect can be reduced either by decreasing the temperature or by using materials with a low work function for the cavity walls [17].

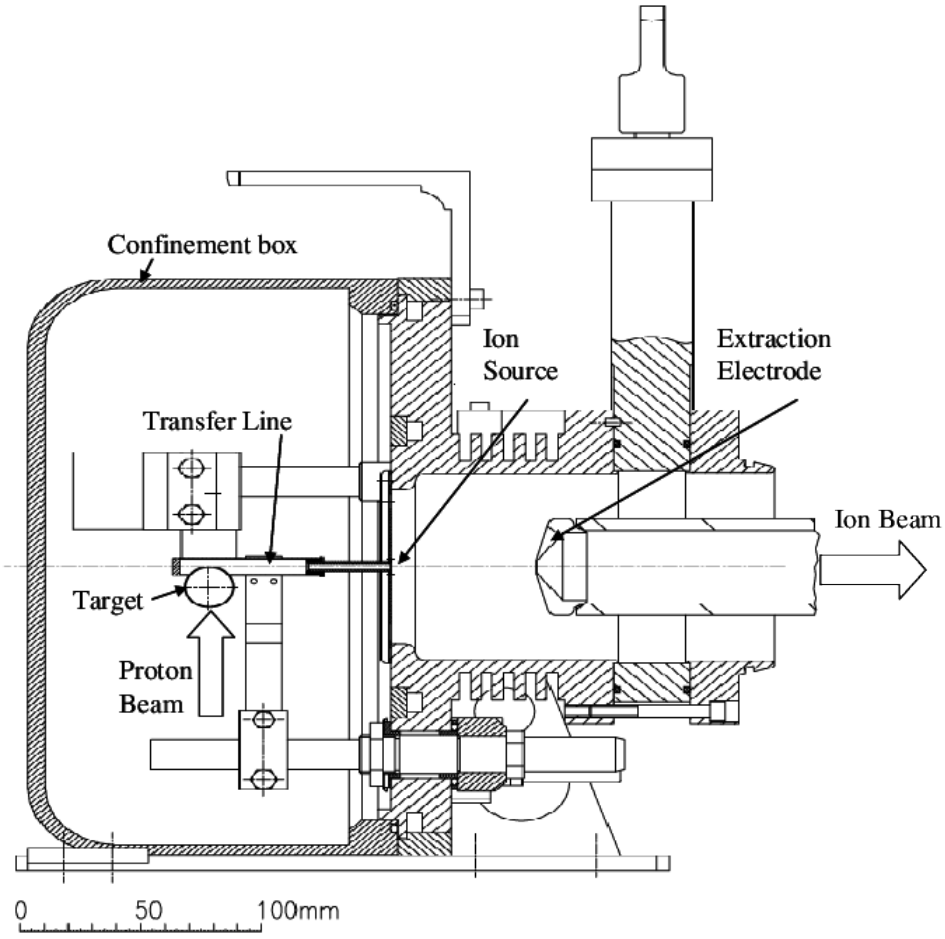

Figure 3.5: A schematic showing the ISOLDE target and ion source [20]. The direction of the proton beam incidence and the direction of the ion beam are shown in arrows.

3.3 PISA

The off-line period of ISOLDE is a good opportunity to develop new ionization schemes at RILIS since the workload does not include setting up and operating the lasers for experimental runs. With that being said, even during the off-line period, a target/ion-source assembly would need to be prepared with the required element and the mass separator would require setup. This requires a large group of people and needs to be scheduled with other machine developments, so time slots can be rather short and hard to come by. For this purpose in the reference area of the RILIS lab one can find the compact Photo-Ionization Spectroscopy Apparatus (PISA). The PISA was designed by T. Kron as a part of his diploma thesis [16].

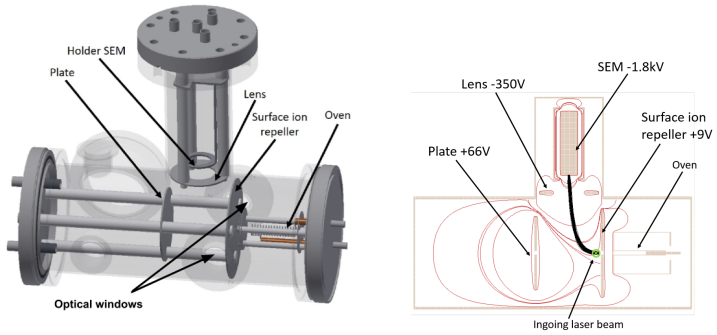

Figure 3.6: On the left: A simplified schematic of the PISA which shows the optical windows for the laser beam, the oven, the SEM holder and the ion optics. On the right: A simulation of the ion trajectory into the SEM with the lines representing the fields created by the ion optics and the typical voltage of each element shown next to its label. Both the drawing and the simulation were created by T. Kron [16].

The PISA is a compact T-shaped vacuum chamber with a resistively heated oven, ion optics and a secondary electron multiplier (SEM) for ion detection. A schematic of the aparatus is shown in Figure 3.6 below.

The main elements of the PISA are:

- **Oven** - Resistively heated oven that holds the sample of the element that will be studied.
- **Surface ion repeller** - Positively charged electrode for repelling the surface ions from the oven away from the extraction region which improves the signal-background ratio.
- **Plate** - Positively charged plate that changes the trajectory of the ions to guide them into the detector area.
- **Lens** - Negatively charged ion extractor that focuses the ions into the SEM.
- **SEM** - Secondary electron multiplier for detection of the ions from the company MasCom Technologies GmbH, model MC-217.

The setting up of the PISA for scheme development is comprised of the following steps:

- A sample with the element of interest is prepared and inserted into the oven. The vacuum pump is set up to create vaccum in the PISA of the order 10^{-6} mBar.

- The laser beams are optimized on position through irises just before the PISA making sure that the beams are not hitting any surface inside the chamber, but are coming out of the back window.
- Once an ion signal is seen, the overlap in position and timing of the laser beams is optimized on it as well as the voltages of the ion optics. The temperature of the oven is also optimized so that the sample is not evaporated too quickly and the ion signal is stable.
- A laser wavelength scan is done for each already known step to make sure that it is as expected from literature and that there is a resonance.
- The spectroscopy can commence by means of e.g. a search for an alternative second excitation step, a search for auto-ionizing steps or spectroscopy of the Rydberg series for the study of the ionization limit.

3.4 UV generation problem

RILIS is the only laser ion source currently that uses both Ti:Sa and dye lasers. While that provides a very good coverage of the spectral range, a recurring problem with the generation of stable UV has been observed. The usage of the dye lasers in conjunction with UV generation leads to a gradual power drop of the UV beam and visible white deposits (analyzed in the past and determined to be carbon) on the UV optics. In addition to the visible deposits on the optics, the UV power measured directly after the crystal is also dropping. This is caused by deposits on the UV generating crystal itself. However, the deposits on the crystal surfaces are minuscule, due to the fact that the laser beam which is frequency doubled to the UV is stronlgy focused into the crystal and the exiting UV beam therefore is small ($< 100\,\mu m$) in diameter. Cleaning of these non-linear crystals can cause damage and/or absorption of water into them. By displacing the laser beam on the crystal, power can be regained in full. Since most of the RILIS ionization schemes use a UV step (see Figure 3.8), it was important to look into this problem as the power drop, induced by the deposits, requires cleaning of the optics up to every few hours which would often mean that someone from the RILIS team has to come in at night only for this purpose. Additionally, if the power drops too much, then the PSD in the beam diagnostics system cannot detect the laser beam and therefore the position stabilization of the beam no longer works.

Figure 3.7: Deposits on mirrors with UV reflective coating caused by 200 ml of Styril 8 (in ethanol and DMSO) and Rhodamine 101 (in ethanol) dye solutions in proximity to 50 mW of UV laser beam at 217 nm. After final assessment, it is clear that the deposits were caused by the DMSO in which the Styril 8 had been dissolved.

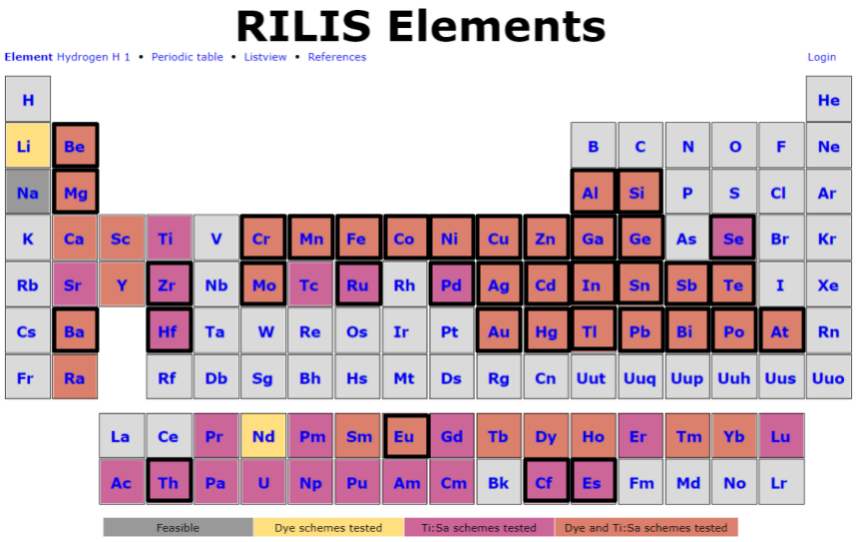

Figure 3.8: The periodic table of elements as shown in the RILIS database [9]. The elements contoured in black indicate the use of at least one UV step in their ionization schemes.

Since it is known that the high energy UV photons break up organic molecules [18], it is reasonable to look for a source of organic molecules in the lab that are volatile enough and present in large quantities. Since the UV was uncharacteristically stable after the initial setup at the end of the year 2020, a conclusion was drawn that this had to do with the fact that the dye lasers in the lab have not been operated for well over a year. This uncharacteristically long time without the usage of dye lasers was caused by the so-called Long Shutdown 2 (LS2) during which no protons were available

at CERN from the end of the year 2018 until the middle of the year 2021.

In order to cover the full range between 210nm and 950nm, RILIS uses Ti:Sa and dye lasers with the option of frequency mixing. The organic dyes that are used for the different spectral ranges include:

- DCM
- Rhodamine B
- Rhodamine 6G
- Rhodamine 101 (640)
- Pyromethene 580
- Pyromethene 597
- Styril 8
- Pyridine 1
- Phenoxazone 9
- Fluorescein 548

They are dissolved in either ethanol or DMSO (Dimethyl sulfoxide) or a mix of the two in order to move the peak of the spectral coverage of the dye and are pumped through circulators. The tuning curves of the dyes can be seen in Appendix A .

In order to isolate the cause of the problem a UV laser with $\lambda = 217\,\mathrm{nm}$ with around 50 mW of power was set up in the RILIS laser laboratory. The UV is generated by frequency quadrupling of the fundamental Ti:Sa: First the light is frequency doubled through a BiBO crystal inside the Ti:Sa cavity and subsequently doubled again, this time outside the cavity, with a BBO crystal. Both of these crystals are very sensitive to moisture and temperature variations. In order to make sure that the UV power fluctuations are not caused by UV deposits, both the powers of the blue and the UV were measured. As mentioned before, at the beginning of these measurements the dye lasers had not been turned on for well over a year, due to the LS2 and the UV power was stable with no deposits visible on the optics even after several days of UV-generation.

In order to test each dye, a beaker of about 200 ml of dye solution was introduced in close proximity to the quadrupling crystal and the UV-reflective optics. Each dye was tested separately with enough time between tests to ventilate the air in the laser laboratory. A powerful air extractor in the entrance area of the lab is used to quickly circulate the air.

Some of the dyes produced considerable deposits with significant power drop of the UV power while others did not produce any deposits and no

power drop was observed during the same measurement period. In order to determine whether the cause was due to the UV breaking up the organic dye molecules or the solvents, pure ethanol and DMSO without any dye admixture was tested. The results convincingly showed that the ethanol did not cause any effect on the UV power, however the DMSO caused very strong deposits and a substantial drop of power of the UV beam.

In order to confirm that the DMSO is causing the problem, the tests were repeated with a special focus on the air quality of the lab between tests and by testing both solvents with the same dye (namely DCM since it is one of the most commonly used at RILIS and is frequently used with both solvents). The results showed no change when DCM is used with ethanol and once again big power loss and deposits when DCM is used with DMSO.

After concluding that the UV generation problem is caused by the use of DMSO in the dye lasers at RILIS, tests were performed to solve the problem. It is convincingly evident that even very small amounts of DMSO in the air cause a problem. The tests were performed with 200 ml solutions with small admixtures of DMSO in the etahnol (10:90) whereas the amount of dye solution pumped through the circulators of the dye lasers is around 1.5 L.

Since one of the most frequently used dye solutions at RILIS is indeed DCM in DMSO, solutions promoting the removal of DMSO from the lab were explored. Tests were performed with sealed circulators (three different models) to check whether the problem is caused by the leakage from the circulators or rather the process of dye changes by the RILIS team during operations. While the circulators where thoroughly checked and fixed in order not to have leaks, it seems that they are not air-tight and DMSO molecules still penetrate the air. In that case, the current solution of the UV generation problem is not to use DMSO. The spectral range gap that the DCM in DMSO leaves can be covered by other dyes, mostly fully covered by Phenoxazone 9 in ethanol (used regularly during the 2021 on-line period). A long-term solution would be to develop a more efficient ventilation system in the lab that can quickly clear out the air. The running period of 2021 showed much improved conditions for the UV-generation at RILIS. Nevertheless, after one to two days, small drops in UV-power were still observable. These have been shown to result from deposits on the UV generating crystal (regaining the power by moving the crystal). This can be explained by the high power density at the exciting surface of the crystal and some lingering remains from the DMSO tests performed at RILIS. It is expected that this effect will disappear over time when DMSO is no longer used.

4 | Lead and cadmium scheme development

This chapter discusses the scheme development which was performed for lead and cadmium at RILIS. The schemes were first tested in the PISA and after choosing a new scheme, it is tested in the ion source of ISOLDE and compared against existing schemes. Scheme development often requires the testing and comparison of several schemes which can take quite a bit of time. However, if the initial schemes are tested off-line (in the PISA), this gives the RILIS team the opportunity to use the available beam-time of ISOLDE more efficiently. The scheme development cannot be performed solely in the PISA however, because the ion source geometry of the apparatus is different to the ion source at ISOLDE and it is important to reproduce the on-line conditions as best as possible in order to get an accurate measure of the scheme's efficiency.

4.1 Lead

The scheme that was used for lead ionisation at RILIS in the past has three steps. The first step is from the $6s^2 6p^2(\frac{1}{2},\frac{1}{2})_0$ ground level to the $6s^2 6p 7s(\frac{1}{2},\frac{1}{2})^o_1$ level at $35287.224\,\mathrm{cm}^{-1}$ with a frequency tripled Ti:Sa laser with $\lambda_1 = 283.39\,\mathrm{nm}$. The second step is to the $6p8p(\frac{1}{2},\frac{3}{2})_2$ level at $51943.9\,\mathrm{cm}^{-1}$ with a dye laser with $\lambda_2 = 600.36\,\mathrm{nm}$. The final step is non-resonant ionization with $\lambda_3 = 532\,\mathrm{nm}$ over the ionization potential which lies at $59819.7\,\mathrm{cm}^{-1}$ (see Figure 4.1). The maximum efficiency of this scheme has been given as 3.1% [36].

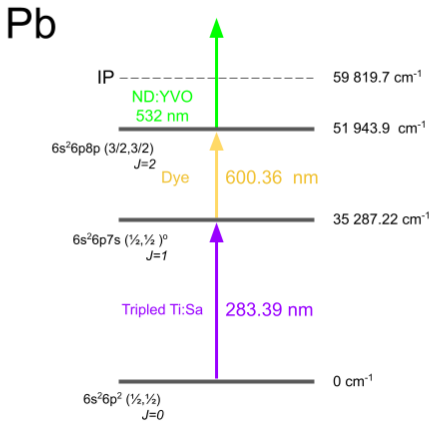

Figure 4.1: Old RILIS scheme for Pb with UV first step, dye second step and non-resonant ionization.

The motivation for developing a new scheme for lead has several points:

- A new scheme is possible with a different first step with a higher energy from the ground level to the $6s^2 6p(^2P^o_{1/2})6d[\frac{3}{2}]^o_1$ level at $46068.44\,\mathrm{cm}^{-1}$ with a frequency quadrupled Ti:Sa laser with $\lambda_1 = 217\,\mathrm{nm}$. This step is closer to the ionization potential and thus, ionization could be possible within the fundamental wavelength curve of the Ti:Sa laser.
- Replacing the old scheme that uses Ti:Sa and dye lasers with a new one that only uses Ti:Sa lasers would require less maintenance during runs as long as it does not compromise on efficiency.
- A full Ti:Sa scheme also helps to reduce the amount of dye used at RILIS (see section 3.4).
- The low efficiency of the current lead scheme used at RILIS could be due to losses into a dark state (see subsection 4.1.4). It is a possibility to repump from a dark state to minimize losses into it and improve the efficiency (see Figure 4.2).

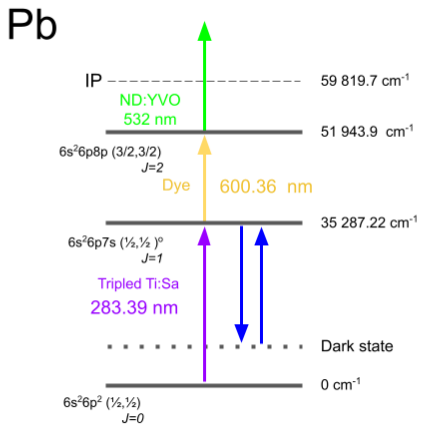

Figure 4.2: Schematic showing the old RILIS ionization scheme of lead with decay into a dark state and repumping from it back to the first excited state in order to (possibly) improve the ionization efficiency.

Several schemes were tested offline in the PISA (see section 3.3). Out of those, the ones with the biggest enhancement over the first step were chosen to be tested in-source.

4.1.1 Two-step schemes

The first and most simple scheme in search for auto-ionizing states that was tried is with the previously mentioned first step at 46068.44 cm^{-1} with $\lambda_1 \approx 217\,\mathrm{nm}$ and a scan with the grating Ti:Sa laser above the ionization potential (at 59819.7 cm^{-1}) in the range 730-750nm (see Figure 4.3). This would be the ideal case for a new scheme, because it uses only two steps - both within the Ti:Sa range. A full Ti:Sa scheme is easier to set up and requires less overall laser maintenance during a run since the dye lasers would require dye changes and since often times the RILIS team has very limited time between runs to switch between different schemes. Avoiding using a dye laser in the same scheme as a UV laser is also one of the solutions to the UV generation problem whenever completely removing DMSO as a solvent is not feasible (see section 3.4).

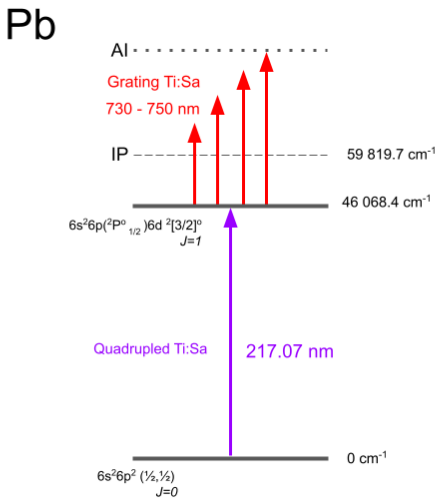

Figure 4.3: Schematic representation of a scan over the first step with a grating Ti:Sa laser in the range 730-750 nm in the search of a directly accessible AI.

No auto-ionizing states were found. However, as is expected, there are multiple Rydberg series that converge towards the ionization potential (see Figure 4.4).

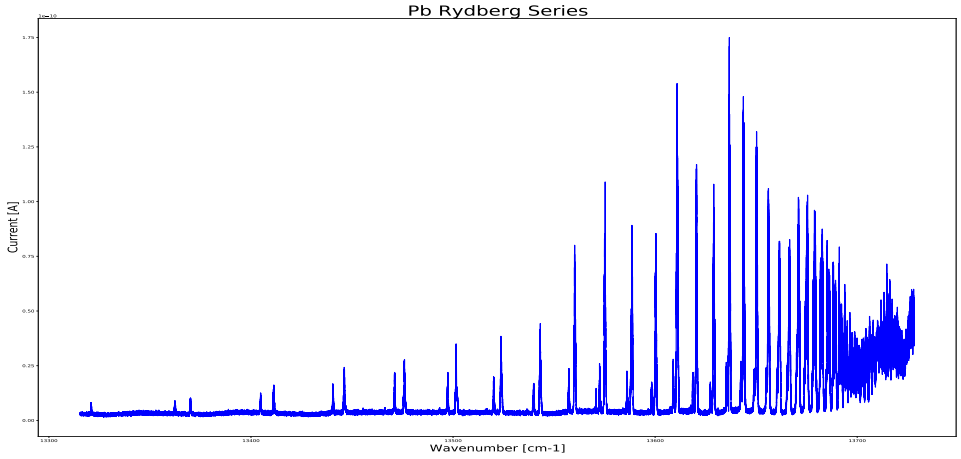

Figure 4.4: A scan over the second step wavelength with a Ti:Sa laser in the range 730-750nm showing Rydberg series with convergence to the IP.

The next performed scan utilized lower wavelengths in order to probe a spectral range higher above the IP. However, to reach a higher energy and scan in the range 560-595nm, a dye laser must be used. A scan in that range with Pyromethene 597 also showed no auto-ionizing states (see Figure 4.5).

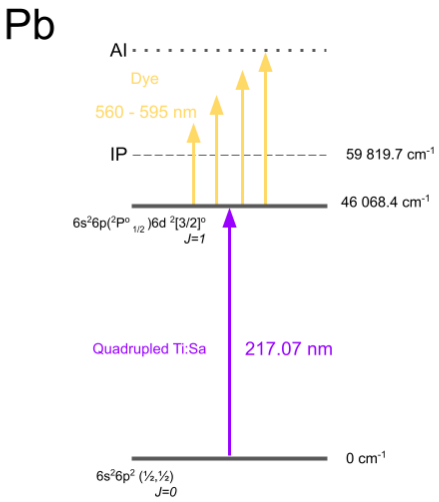

Figure 4.5: Schematic representation of a scan over the first step with a dye laser with Pyromethene 597 dye in the range of 560-595 nm.

4.1.2 Three-step schemes

Since no auto-ionizing states were found by scanning of the second step wavelength, a search for an auto-ionizing state with an even higher energy would require an additional, intermediate step to scan over. The step that was chosen is a state from the Rydberg series which had the highest intensity in the scan at 13636.7 cm^{-1} (see Figure 4.6).

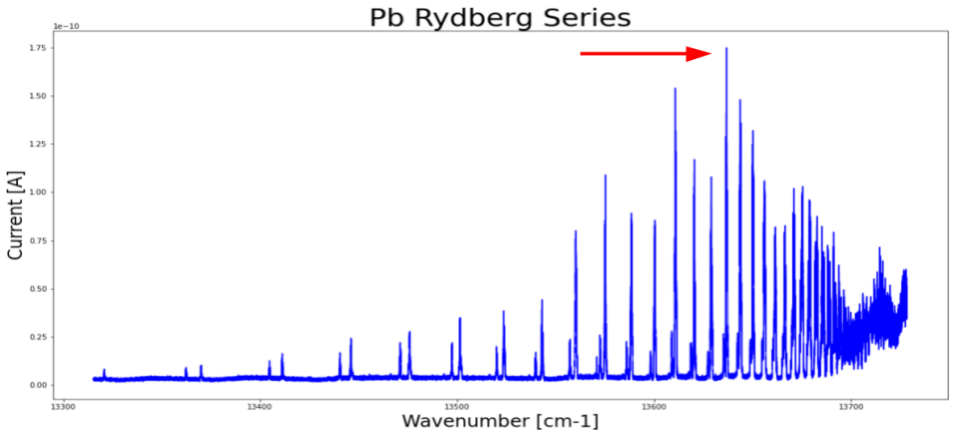

Figure 4.6: Rydberg series with red arrow indicating the level chosen as a second step.

To reach the second step, another Ti:Sa cavity is set up with 733.3 nm

which is within the fundamental range of the Ti:Sa. The three-step scheme with a scan with the grating Ti:Sa over the second step is shown schematically in Figure 4.7.

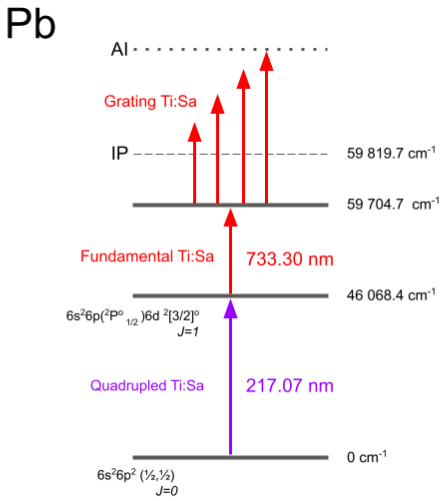

Figure 4.7: Schematic representation of a scan over the second step with a grating Ti:Sa laser.

No auto-ionizing states were found through this scan. Another scan was done over the same second step with a dye laser to reach higher above the ionization potential (see Figure 4.8), but led to no discovery of AIs either.

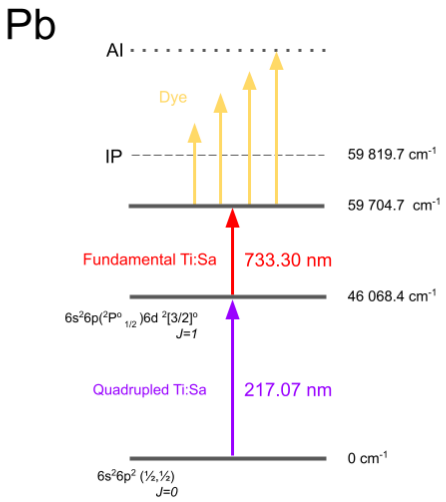

Figure 4.8: Schematic representation of a three-step scheme scan with dye laser

Since no auto-ionizing states were found, the next step was to find the best possible second step and to subsequently ionize (non-)resonantly. After careful literature searches, a different Rydberg state to the one previously used was chosen. This was due to the fact, that past experiments showed that auto-ionizing Rydberg series leading to an excited ionic state in lead exist [13–15]. Since the first step used in all of these previous experiments was the one leading to the $6s^2 6p7s_1^o$ level at 35287.22 cm^{-1} with 283.39 nm, a comparison of the Rydberg levels reached was performed. It was found that from the 217 nm - transition, the same Rydberg level could be reached with 867.3 nm (fundamental Ti:Sa) instead of 448.2 nm. A scan was done over ionic Rydberg states found in literature [13] [14] [15]. The second and third steps tested are shown in Table 4.1. The comparison between them is made by directly measuring the enhancement that the third steps give over the second with the laser on/off effect of the third step. As can be seen, a second step with 11530.14 cm^{-1} and a third step with 12151.50 cm^{-1} gives a factor 17 enhancement which is the best out of all of the combinations shown.

Second step [cm^{-1}]	Third step [cm^{-1}]	Enhancement over second step
11 192.23	17 384.00	2.8
11 249.30	17 087.30	3.3
11 361.27	17 087.23	3.5
11 530.14	17 087.23	1.4
13 636.68	17 087.23	1.2
11 530.14	12 951.50 (resonant)	17
11 530.14	12 949.70 (resonant)	13

Table 4.1: The table shows the second and respective third steps that were tested and compared. The last two rows show resonant third steps leading to auto-ionizing Rydberg states in the ion.

4.1.3 In-source scheme comparison

The final scheme chosen to compare against existing ones has a first step from the ground level to the $6s^2 6p(^2P^o_{1/2})6d[\frac{3}{2}]^o_1$ state at 46068.44 cm^{-1} with a frequency quadrupled Ti:Sa laser with $\lambda_1 = 217.07$ nm. The second step is to the $6s^2 6p7p(\frac{3}{2}, \frac{1}{2})_2$ level at 57598.6 cm^{-1} with a fundamental wavelength Ti:Sa laser with $\lambda_1 = 867.29$ nm. The ionizing step is also in the fundamental Ti:Sa range with $\lambda_1 = 772.19$ nm to a resonant state at 70548.7 cm^{-1}. It was tested in-source at the ISOLDE frontend and directly compared with the old RILIS scheme [9] and the scheme developed in the ARIEL facility in TRIUMF, Vancouver [8] (see Figure 4.9). It is crucial to test the scheme in-source since the geometry of the ion source is different than the geometry of the PISA and the aim is to reproduce the on-line operations environment as best as possible.

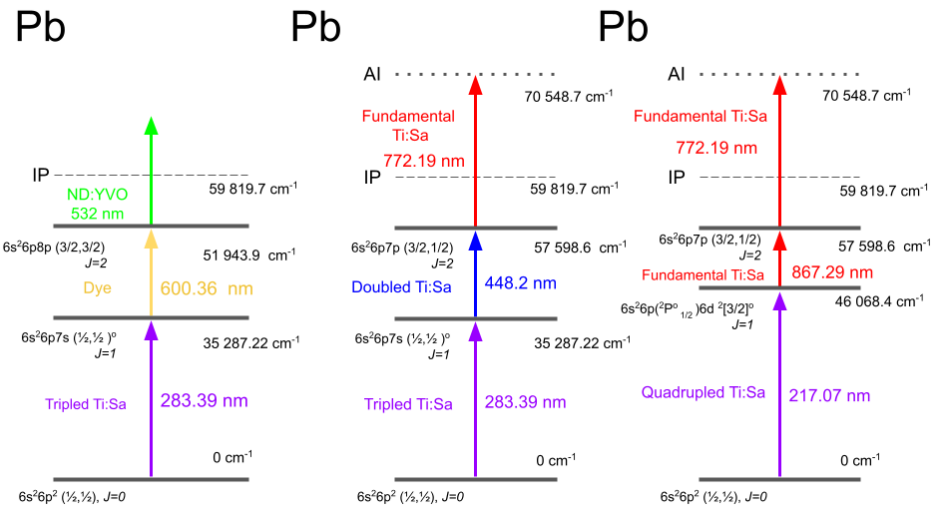

Figure 4.9: The three schemes that are compared for efficiency: old RILIS scheme with dye step, full Ti:Sa scheme from TRIUMF and new RILIS scheme.

In the end, the new RILIS scheme shows to be the most efficient of the three and a factor of at least 10 better than the old RILIS scheme. This would scale the laser ionisation efficiency to about 30%. A proposal from the COLLAPS experiment in ISOLDE to the INTC from May 2021 suggested using the new ionization scheme to study the "magic" lead isotopes from A = 187 up to A = 208 by high resolution laser spectroscopy [19]. The proposal was accepted and in October 2021 the experiment was performed. The COLLAPS proposal determines the necessary beam-time taking into account the 30% efficiency determined by RILIS through scaling the enhancement of the new scheme. A total of 17 shifts were requested by the COLLAPS experiment (around one week of beam-time). The yields from the new ionization scheme made it possible to perform the tests in about three days which gave the COLLAPS team the opportunity to repeat the tests with most of the isotopes in order to obtain better statistics. This highlights how scheme development at RILIS can directly affect the efficiency of ISOLDE since the ISOLDE run schedule is very busy and an experiment rarely gets more than a week of beam-time. The higher the efficiency of ionization is, the better the yields are and the less beam-time is necessary for an experiment.

4.1.4 Repumping from dark state

A reason suggested for the overall low ionization efficiency of the old RILIS scheme for lead, was decay of population into so-called dark states. A dark state refers to a state which cannot decay back into the ground state

through photon emission and vice versa: it cannot be accessed from the ground state by laser excitation due to the selection rules ($-1 \leq \Delta J \leq 1$ and no parity change). The stored energy can be transferred through other mechanisms (for example through collisions). In the case of lead however, there is a probability for electrons to decay into a dark state by emission of a photon from the excited state used for the first step. In addition to the decay back into the ground state, there are three such dark states that have the right parity and the correct J (see Table 4.2).

Transition	Transition strength [s^{-1}]	Wavelength [nm]	Branching ratio
7 819.26 - 46 068.44	2.2×10^7	261.36	-
10 650.33 - 46 068.44	-	282.25	32%
21 457.79 - 46 068.44	9.2×10^7	406.21	50%

Table 4.2: The table shows the possible transitions from dark states into the excited step used as a first step for the new lead ionization scheme [11]. The branching ratios are taken from [19].

A test performed in conjunction with the laser scheme development was to try and repump from the dark state at 21457.79 cm^{-1} to the first excited state at 35287.22 cm^{-1}. The reasoning behind this is that the branching ratio of that line is around 50% so it is possible that there are significant losses into that state in comparison with the other possible dark states [19]. For the repumping, a frequency doubled Ti:Sa laser was used with $\lambda = 406.21$ nm (see Figure 4.10).

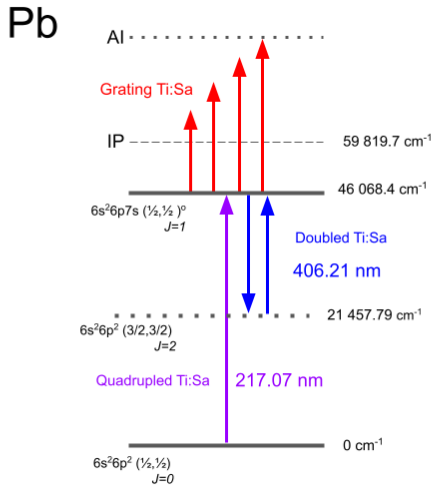

Figure 4.10: A schematic representation of the repumping test performed in the atomic beam unit (PISA).

No enhancement of the signal was seen from the repumping which leads

to the conclusion that no significant losses into this dark state are present. To further confirm that result, the first step has been undersaturated in order to see better an effect of the repumping. That test also shows no effect from the repumping. The only way the dark state could be confirmed, was by delaying the second and third steps in time with respect to the first. This way, time is given to the excited atoms to undergo the decay into the dark state, from where they could be re-excited. In a realistic scenario of RILIS operation, the lasers are overlapped in time and the laser steps saturated, so that no time is given for the atoms to decay into the dark state.

4.1.5 Determination of the first ionization potential of lead

A piece of important information that can be extracted from the data gathered through the scheme development is the value of the ionization potential of an element. This shows that scheme development is not only important for improving the overall efficiency of ISOLDE, but also serves as an opportunity to update or reaffirm the existing data in atomic physics literature.

The first ionization potential of lead as is given in NIST Atomic Spectra Database is $59819.558\,\mathrm{cm}^{-1}$ [39]. In this section, the first ionization potential of lead has been extracted by analysing the observed Rydberg series that converge to it and is compared to the value from literature. All of the data analysis and graphics were done in Python.

Rydberg analysis

The main reason for scanning for Rydberg states was to check whether we can reach the same ones that were used in the ionization scheme from TRIUMF [13] with our new first step and if there is an alternative step within the series that is more efficient. The Rydberg series that can be seen on Figure 4.4 were gathered through four scans and the data has been added together. Since there is a big number of peaks to be fitted, it is more efficient to write a code that cycles through the peaks and fits them rather than doing it manually for every separate peak. Thus, a fitting of the peaks in the four separate data sets has been performed by first locating the peaks and then fitting them automatically. The program finds the peaks using the *find_peaks* function in the SciPy library which finds the local maximum of a data set by comparing neighbouring points [40]. Then, the peaks are fitted with a Gaussian which reproduces the peak shape. The fitting is done with the *curve_fit* function in the SciPy library which uses a non-linear least squares method to fit a specific function to a set of data and the output values are the fit parameters of the function [41].

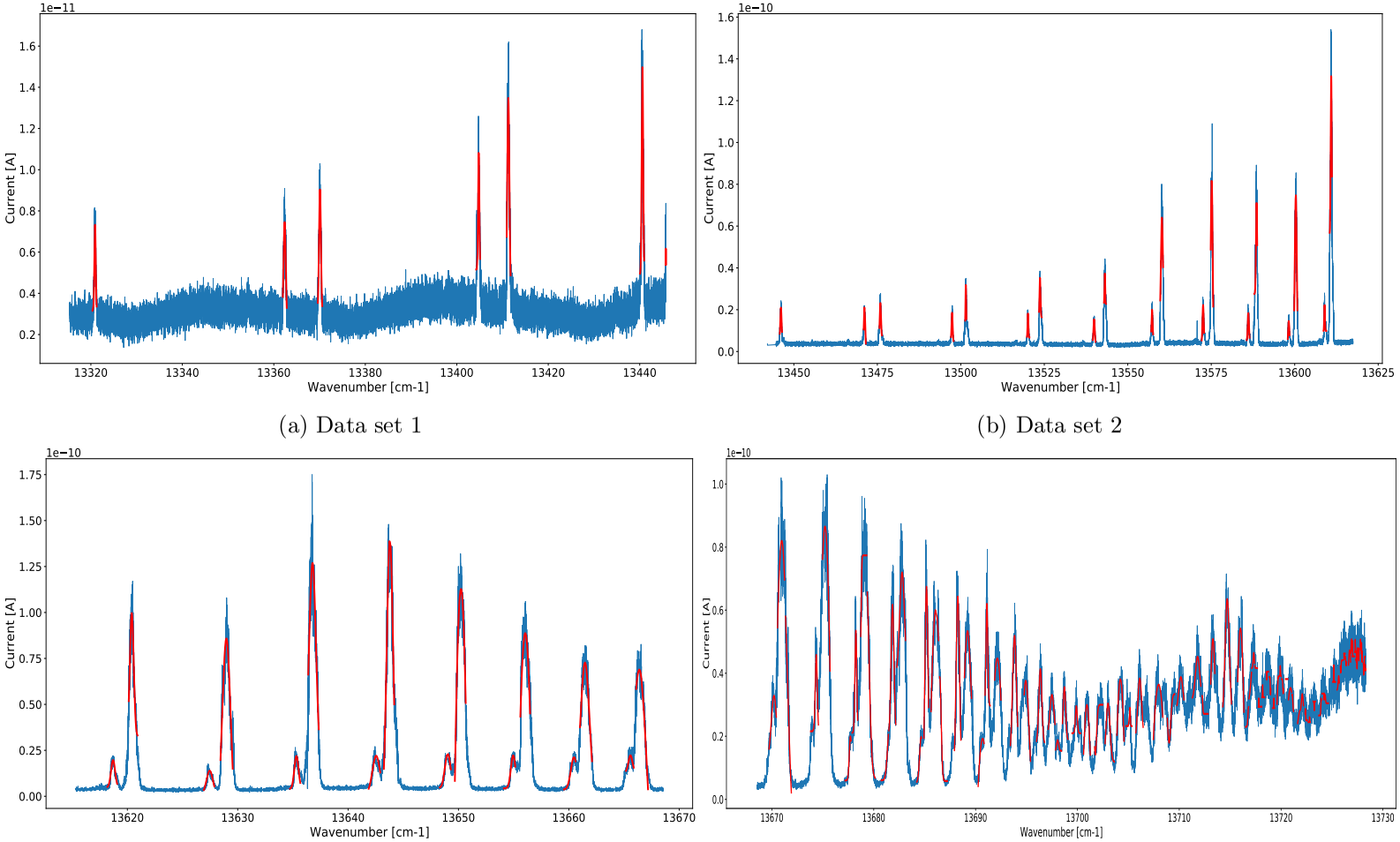

(a) Data set 1

(b) Data set 2

(c) Data set 3

(d) Data set 4

Figure 4.11: Gaussian fit of all of the peaks in the four data sets that were taken. The data from the wavemeter is in blue and the red curve indicates the fit of the corresponding peak.

The output fit curves from the Python code can be seen in Figure 4.11. Comparing e.g. (a) and (d), it can be seen that the peaks at lower wavenumbers (lower energies) are far away from each other which makes the fit better. As the peaks grow closer together as they converge to the ionization potential, it becomes increasingly difficult to distinguish the different peaks and even more so to fit them. As can be seen in Figure 4.11d, the peaks that are closest to the IP are more difficult to distinguish and the program struggles to fit them properly, whilst finding additional artefacts that it considers peaks. The other objects that the code fits which are not well-defined peaks do not skew the data analysis, because later they appear as outliers which can be easily identified and excluded from the calculations as there is enough statistics from the "good" points to calculate the IP. Even if the fit is done peak by peak manually, the final peaks become difficult to fit. The peaks from the different Rydberg series start converging into one another and the final result is therefore almost impossible to attribute to a sole series.

Calculation of the IP

For calculating the IP of lead, Equation 2.34 can be used. The mass-corrected Rydberg constant for ^{208}Pb is known from literature to be 109 737.0262 cm^{-1}. The energies E_n are taken as the mean of the fit curve for each peak in the Rydberg series. Treating the IP as a not yet known value, an initial guess-value of the IP is roughly estimated from Figure 4.4 as the series converge to this energy. The principal quantum number n has to be assigned to each of the Rydberg levels. The quantum defect $\delta(n)$ was calculated by U. Fano et al. for different elements and their different series (s, p, d and f) up to Z=102 [42]. The results are shown in Figure 4.12 with the red line indicating where the values for lead (Z=82) lie.

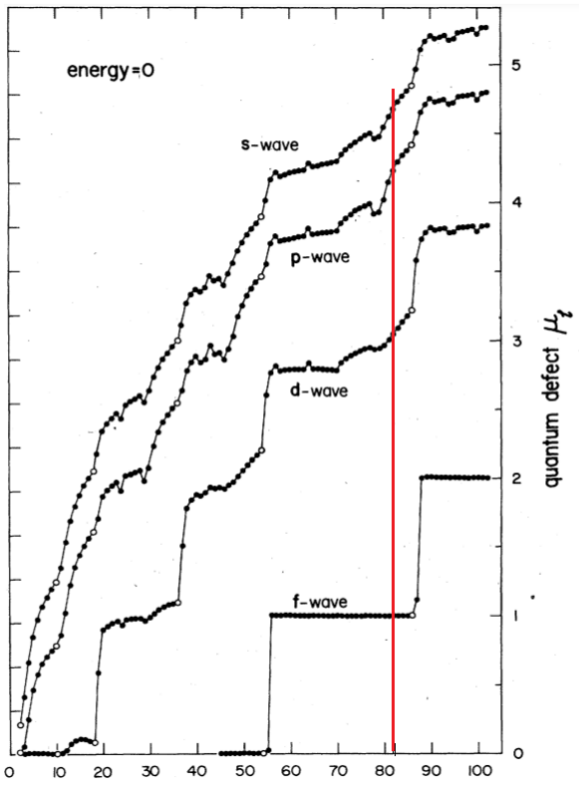

Figure 4.12: Quantum defect values calculated for the s, p, d and f-series for all elements up to Z=102 [42]. Red line added to show the values for lead.

From the original figure, the values of the quantum defects for the different series were extracted for the specific case of lead by image processing with the program ImageJ. The results are shown in Table 4.3.

Series	Quantum defect δ
s	4.68
p	4.25
d	3.04
f	1

Table 4.3: Quantum defect values of the s, p, d and f series extracted for lead (Z=82) from U. Fano et al. [42]

First, from Equation 2.34, $n^\star$ is calculated. Values of n are assigned to the peaks in the Rydberg series. Since n is always an integer, the fractional part of n^* ideally should correspond to the fractional part in one of the values of the quantum defect in Table 4.3. In turn, this helps to identify the series to which a peak belongs as the series overlap and it is not obvious which peak

belongs to which series. The real values of the principal quantum number are then corrected with the integral part of the quantum defect values. Once the quantum defect δ is plotted over n, there are sets of points which are more or less constant (depending on the quality of the initial guess for E_{IP}) which correspond to the different series observed as is shown in Figure 4.13.

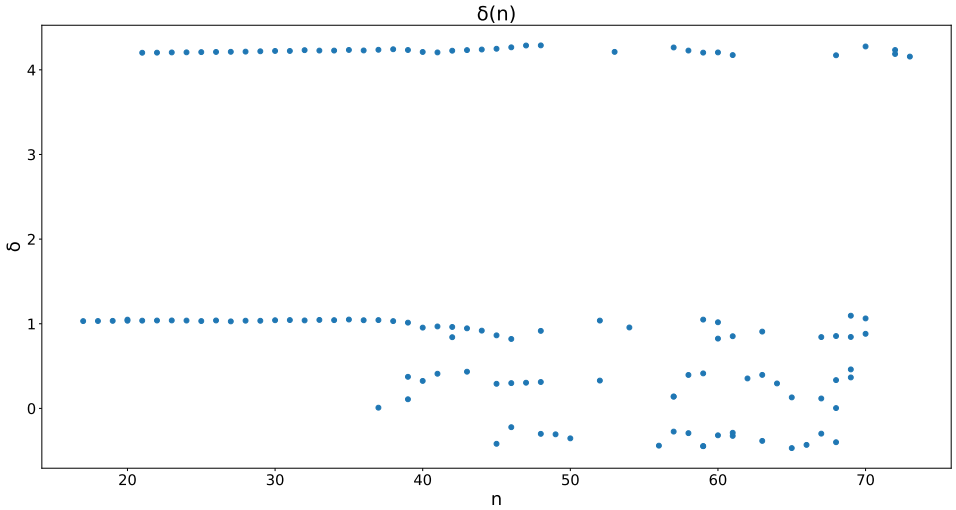

Figure 4.13: The quantum defects δ plotted over the values of the principal quantum number n and E_{IP} assumed as $59819.7\,\mathrm{cm}^{-1}$. Two clear series of points forming linear patterns can be seen which correspond to the f-series (around $\delta = 1$) and p-series (around $\delta = 4.25$).

The f and p-series can be identified as well as some outliers as n gets higher. They are not assigned to a series and are most likely a result of the inaccurate peak fitting very close to the IP since the outer-most electron is in a $6d$ shell. According to the selection rules, it can transition either into a p, f or h shell, where the probability for an h-shell is relatively low and any series belonging to it would be weak. The selection rules allows three transitions for each of the series with different ΔJ, but the strongest transitions can be expected into the p and f shells with a $\Delta J = +1$. The final Rydberg state will ultimately be annotated by [Xe]$6s^2 4f^{14} 5d^{10} 6p$**5f** or **7p** with $\Delta J = 0$, 1 or 2.

By adjusting the IP value, the dependence between the quantum defect and the principal quantum number should become increasingly close to a constant as the IP gets closer to the actual value.

Once the series have been identified, their energies are plotted over n and are finally fitted according to Equation 2.36. The energies are added to the energy of the first step and from the same equation, the IP value is extracted directly. The results are shown in Figure 4.14 and Figure 4.15.

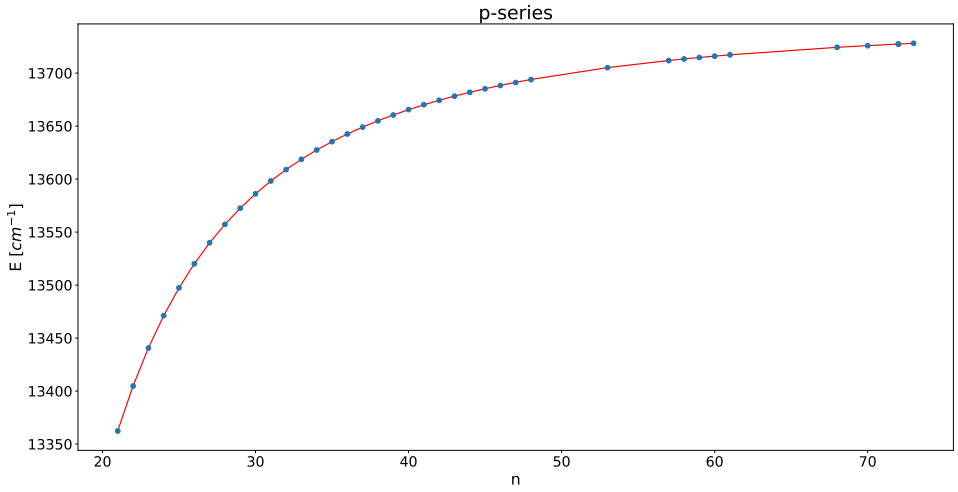

Figure 4.14: The energies of the peaks in the p-series plotted over n. The IP value resulting from the fit is E_{IP}=59819.76(07)(3) cm^{-1}.

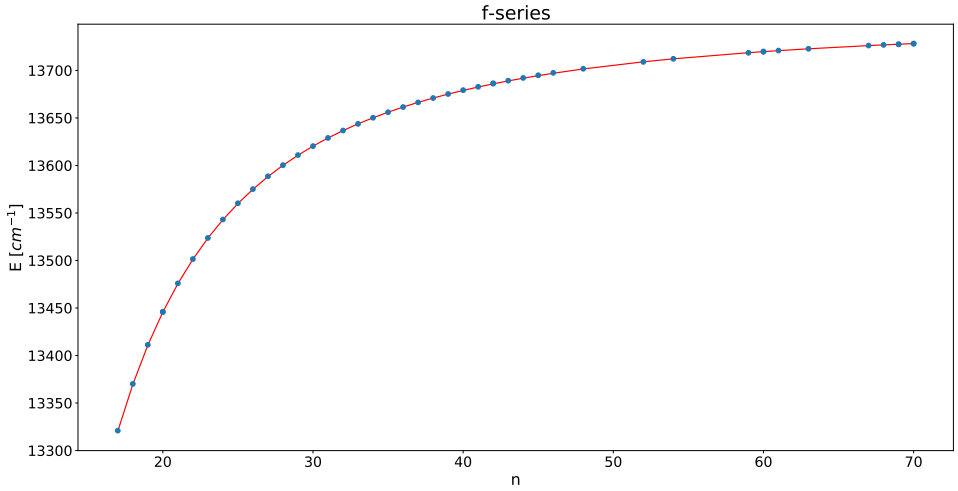

Figure 4.15: The energies of the peaks in the f-series plotted over n. The IP value resulting from the fit is E_{IP}=59819.83(2)(3) cm^{-1}.

The value for the IP that is known from literature is 59 819.558(5) cm^{-1} [39]. Comparing with the values obtained in this analysis, it can be seen that the real value is within the fitting error. The accuracy of the value can be improved by improving the fit of the peaks close to the IP e.g. by fitting them manually. However, since there is no mass selectivity in these measurements, the final value will always be a convolution between the different stable isotope masses of lead.

Considerations for calculating the uncertainty

In order to calculate the final uncertainty of the IP value, there are different error considerations that need to be taken into account. The error of the wavemeter which was used for the scans is $\Delta_{WM} = 0.03\,\mathrm{cm}^{-1}$. Additionally, there is an uncertainty in the value of the first step which is taken from NIST $\Delta_{E1} = 0.0013\,\mathrm{cm}^{-1}$ [5]. The statistical uncertainty is first taken from the initial fits of the Rydberg peaks. The standard deviation is taken directly from the *curve_fit* function as it is one of the output parameters. These standard deviations are then used as input uncertainties in the final fit of the p and f-series. This is necessary in order to make a weighted fit that takes into account the difficulty of fitting the higher-energy peaks close to the IP. The wavemeter error is added to the error of the first step which gives $\Delta_{WM} + \Delta_{E1} = 0.03 + 0.0013 = 0.0313\,\mathrm{cm}^{-1}$. The values of the IP are given with two decimal numbers so rounding the value for the uncertainty in the same way gives $0.03\,\mathrm{cm}^{-1}$. The uncertainty of the first step energy value is small enough that it ends up not contributing. Finally, the uncertainty of the IP value that has been calculated is the wavemeter error - $0.03\,\mathrm{cm}^{-1}$ and the propagated statistical error - $0.02\,\mathrm{cm}^{-1}$ for the f-series and $0.007\,\mathrm{cm}^{-1}$ for the p-series.

4.2 Cadmium

The current scheme used at RILIS for the ionization of cadmium has a first step from the $5s^2\,{}^1S_0$ ground state to the $5s5p\,{}^1P_1^o$ state at $43692.47\,\mathrm{cm}^{-1}$ with a frequency tripled Ti:Sa laser with $\lambda = 228.87\,\mathrm{nm}$. The second step leads to the $5s5d\,{}^1D_2$ level at $59219.82\,\mathrm{cm}^{-1}$ provided by a dye laser with $\lambda = 644.02\,\mathrm{nm}$. The ionization potential lies at $72539.90\,\mathrm{cm}^{-1}$. The ionization step is non-resonant with the $\lambda = 532\,\mathrm{nm}$ Blaze Nd:YVO laser (see Figure 4.16).

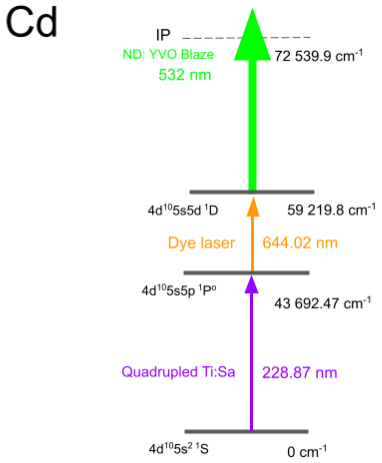

Figure 4.16: Cadmium scheme used currently at RILIS. Image taken from the RILIS database [9].

The motivation to also test a new scheme for cadmium has three main points:

- The literature on cadmium is quite old [4] which warranted a scan over the first step with the grating Ti:Sa and/or dye laser in search of new levels that perhaps have not yet been listed in literature [10] which might be used as second steps in the excitation of the atom. This is plausible due to the developments in laser technology and their subsequent use for laser ionization.
- The first step is in the UV range while the second step uses a dye laser. This is another good opportunity to test the stability of UV generation when dye circulators are used in conjunction. Moreover, since this UV wavelength is higher (thus, the photons have lower energy), it is interesting to see if the effect (if there is one) of the UV on the optics will be the same as the lower wavelengths previously tested (around $\lambda = 217\,\mathrm{nm}$).
- At RILIS, a full Ti:Sa scheme is preferred as long as it does not compromise the ionization efficiency, because the interventions are minimal and therefore the maintenance during operations is easier. Ideally, a second step with a wavelength within the Ti:Sa range would be found to replace the current second step that uses a dye laser.

Schemes tested

Unlike in the Pb case, an alternative first step was not available for Cd. There was not another possible one from literature and a scan for a new one that may not be in literature is redundant since the lower states are usually well studied as they are easily populated e.g. through illumination with broadband light sources and subsequent fluorescence measurements resulting from the decay. Furthermore, it would be quite difficult to scan for one seeing as that would require frequency tripling and/or quadrupling which would be difficult to stabilize as the wavelength changes. In the end, the prevously mentioned first step has been used with $\lambda = 228.87\,\text{nm}$.

Scans were performed first with a frequency doubled grating Ti:Sa for a new second step in the range $398 - 430\,\text{nm}$. This range was chosen as it falls between the wavelengths of known steps [4]. After finding no new alternative second steps (aside from the ones listed in literature), another scan was performed with a dye laser covering a different energy range, but no transitions were found there either. As was the case for the lead (see section 4.1), these tests were carried out in the atomic beam unit (see Figure 4.17.)

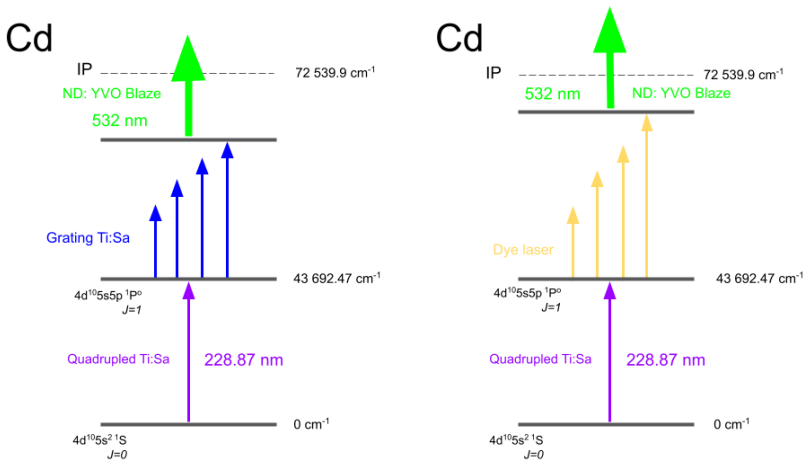

Figure 4.17: Schematic representation of the second step scans performed with grating Ti:Sa and dye laser (Energy levels not to scale).

Since no alternative second steps were found, the next part of the scheme development focused on scanning for autoionizing steps over the already known possible second steps from literature. For that to be done, a comparison between the efficiency of the different schemes is first necessary. The requirements for a second step are three depending on the transition rules and wavelength availability at RILIS:

- The parity of the state has to be even since the level from which it starts has odd parity.

- The ΔJ has to be either -1,0 or 1.
- The wavelength of a photon required for this transition should fall within the (frequency doubled) Ti:Sa spectral range coverage since the goal is to replace the dye laser second step.

There are three possible second steps known from literature that fulfil these requirements. Details can be found in Table 4.4. They were all tested together with non-resonant ionization with a 532nm Nd:YVO laser in the atomic beam unit (see Figure 4.18.)

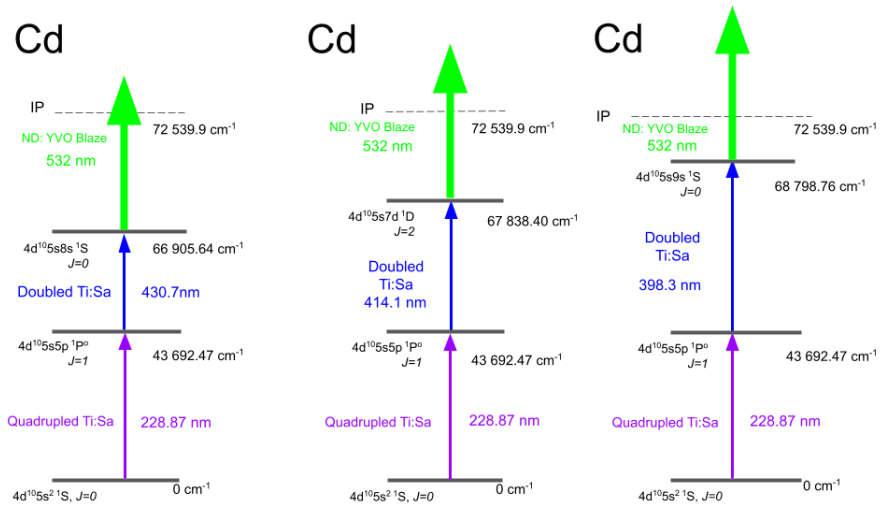

Figure 4.18: Schematic representation of the ionization schemes using different second steps known from literature together with non-resonant ionization into the continuum compared against each other (Energy levels not to scale).

Level energy [cm^{-1}]	Transition $\lambda[nm]$	Configuration	Term	ΔJ
68798.76	398.3	$4d^{10}5s9s$	^1S	-1
67838.40	414.1	$4d^{10}5s7d$	^1D	1
66905.64	430.7	$4d^{10}5s8s$	^1S	-1

Table 4.4: The table shows the second steps tested with non-resonant ionization over the first step. The ΔJ is in relation to the first step, as is the wavelength.

The step with λ=414.1 nm shows the best enhancement of the ion current signal over the first step. This step also has the highest transition strength out of the three tested ($4.7 \times 10^{-6}\,\mathrm{s}^{-1}$) according to the lines on the NIST Atomic Spectra Database [4]. This scheme was then tested against the old cadmium scheme in-source (see Figure 4.19).

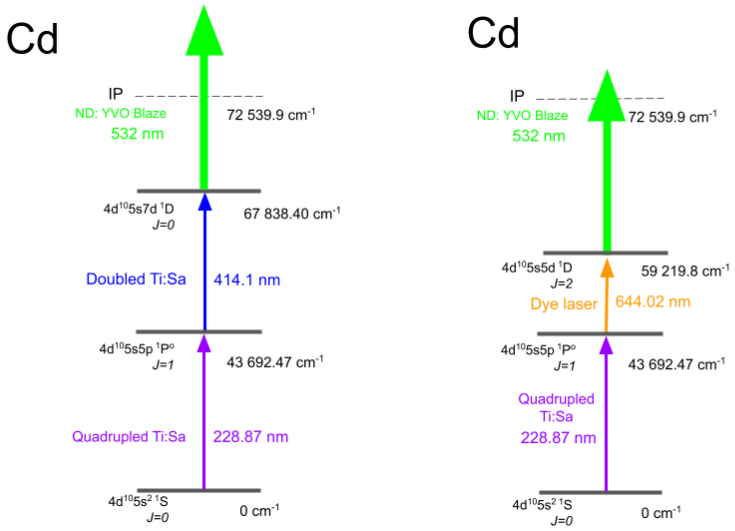

Figure 4.19: Schematic representation of the old RILIS scheme for Cd and the scheme using a new λ=414.1 nm second step compared against each other in the ion source. (Energy levels not to scale).

Comparing these two schemes shows that the old RILIS scheme has better enhancement over the first step. However, a scan for auto-ionizing states was performed with the grating Ti:Sa over the λ=414.1 nm second step in the range 730 - 873 nm. Since a scan for AIs was already performed in the past for the dye laser second step without finding any resonances, it was worth investigating this again for the alternative second step. If an AI can be found, the overall efficiency of the scheme might be higher in spite of a lower enhancement of the second step (see Figure 4.20).In addition, other effects like heating with the high-power 532nm laser can be circumvented when using an AI, oftentimes improving the signal to background levels.

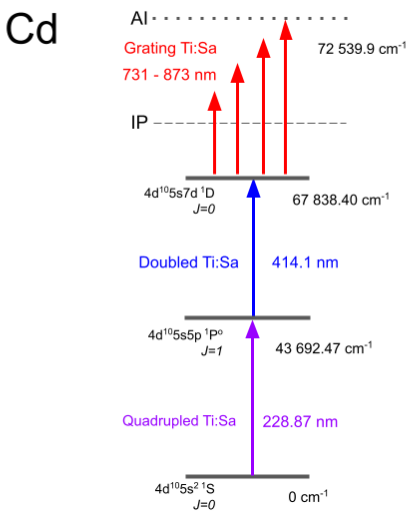

Figure 4.20: Schematic representation of a scan for auto-ionizing states over the λ=414.1 nm second step in the range 731 - 873 nm. (Energy levels not to scale).

No auto-ionizing states were found within the scan range. A saturation measurement was carried out in order to have a rough idea at what power the 414 nm transition saturates in the geometry of the ion source. The reason for this is to make sure that the signal enhancement is not a result of another effect (e.g. a power effect). The measurement is done by putting in optical ND (Neutral Density) filters into the laser beam in order to reduce its power. The saturation curve can be seen on Figure 4.21.

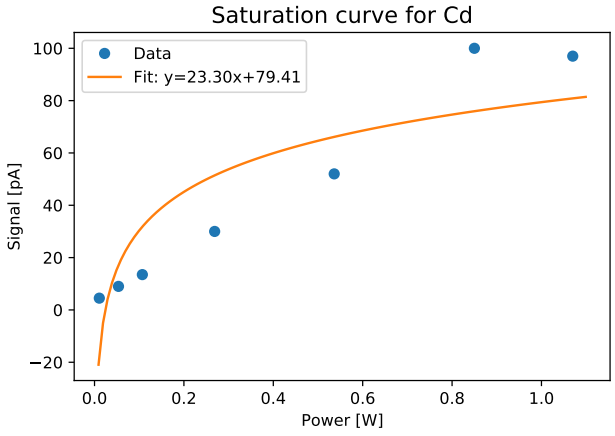

Figure 4.21: Saturation curve that shows the ion signal dependence on the power by changing the power through optical filters in the laser beamline.

5 | Conclusion

Within this work, three projects have been presented:

- The production of a stable UV laser beam at RILIS has been improved by discovering the source of instability. The UV laser beam breaks up the organic molecules from the solvent DMSO used for the dye lasers and leads to build-up on the UV optics leading to a substantial power loss over a short period of time. Since the cause of this issue has been discovered, DMSO has been removed from the RILIS laser room. The range which is covered by the dyes dissolved in DMSO can be covered by other dye-solvent combinations. Due to the UV stability, new possibilities for scheme development have been explored, reaching lower wavelengths than feasible before. Two examples of such schemes are the main focus of this work.

- The most extensively discussed result in this thesis is the development of a new ionization scheme for lead. The new scheme is around ten times more efficient than the previously used scheme at RILIS. It is also a full Ti:Sa scheme which is overall easier to set up and maintain during operations. The new scheme has already been used in the COLLAPS experiment in ISOLDE and due to the high ionization efficiency, the estimated beamtime necessary for collecting data was reduced by half giving the opportunity to repeat the tests and improve the statistics of the experimental data. The full process from developing a new scheme and making it available to the ISOLDE users to the COLLAPS experiment using it during its data collection has taken less than a year. Alongside the development of a new scheme, the first ionization potential of lead has been calculated and compared to the existing values in literature.

- Scheme development for cadmium has also been carried out. The known literature on cadmium was published before the currently used laser technologies were fully developed which served as an opportunity to search for new energy levels that possibly were not previously accessible through laser ionization. Ultimately, new levels were not discovered through laser scans. The levels known from literature that

could serve as an appropriate second step over the previously used first step have been tested to check if the overall efficiency improves. The tests show that the previously used RILIS scheme is the most efficient one so it has not been updated.

A | Laser dye tuning curves

The page below shows the emission curves for different laser dyes for two wavelengths of the pump laser. The dye is chosen depending on the wanted wavelength of the laser output light (the pump laser wavelength should also be taken into consideration). The range of wavelengths that a dye covers depends on the solvent which is used. Substitution of the solvent or mixing solvents results in a range shift for the curves. The tables show the efficiency of these dyes and the necessary concentration of the dye in the solvent. This data is provided by the dye laser manufacturer (in this case Sirah Laser- und Plasmatechnik GmbH).

355 nm

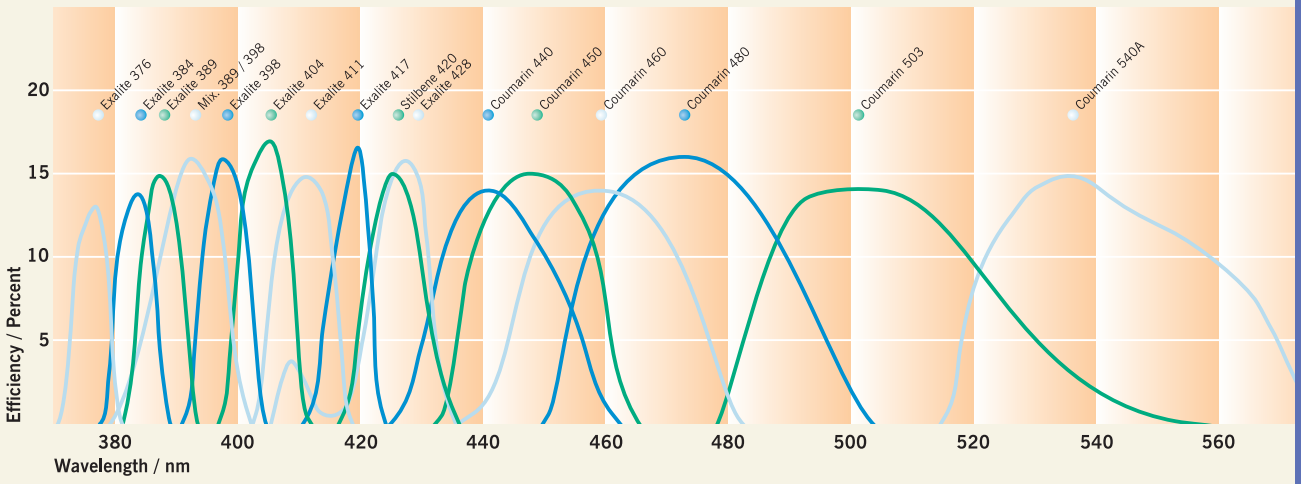

Name	Peak (nm)	Range (nm)	Efficiency	Solvent	Concentration (gram/liter)	Comment
Exalite 376	377	372 .. 380	13 %	p-Dioxane	0.90	
Exalite 384	384	379 .. 388	14 %	p-Dioxane	0.30	
Exalite 389	387	382 .. 392	15 %	p-Dioxane	0.20	
Mix. Exalite 389 / 398	393	382 .. 401	16 %	p-Dioxane	0.10 / 0.10	
Exalite 398	398	393 .. 403	16 %	p-Dioxane	0.18	
Exalite 404	405	399 .. 410	17 %	p-Dioxane	0.15	
Exalite 411	411	404 .. 417	15 %	p-Dioxane	0.14	
Exalite 417	419	413 .. 422	17 %	p-Dioxane	0.20	
Stilbene 420	425	419 .. 434	15 %	Ethanol + H_2O	0.22	Stilbene 3
Exalite 428	427	419 .. 434	16 %	p-Dioxane	0.15	
Coumarin 440	441	429 .. 460	14 %	Ethanol	0.25	Coumarin 120
Coumarin 450	448	434 .. 463	15 %	Ethanol	0.20	Coumarin 2
Coumarin 460	460	442 .. 479	14 %	Ethanol	0.25	Coumarin 47
Coumarin 480	473	452 .. 500	16 %	Ethanol	0.40	Coumarin 102
Coumarin 503	500	480 .. 540	14 %	Ethanol	0.40	Coumarin 307
Coumarin 540A	535	517 .. 574	15 %	Ethanol	1.60	Coumarin 153
Rhodamine 590	574	563 .. 597	14 %	Ethanol	0.40	Rhodamine 6G
Pyrromethene 597	585	571 .. 612	12 %	Ethanol	0.32	
Kiton Red 620	596	582 .. 620	13 %	Ethanol	0.30	Sulforhodamine B
Rhodamine 610	600	588 .. 632	13 %	Ethanol	0.35	Rhodamine B
Rhodamine 640	630	621 .. 674	14 %	Ethanol	0.50	Rhodamine 101
DCM	640	605 .. 665	13 %	Ethanol	0.30	
LDS 698	693	664 .. 722	9 %	Ethanol	0.45	Pyridine 1

532 nm

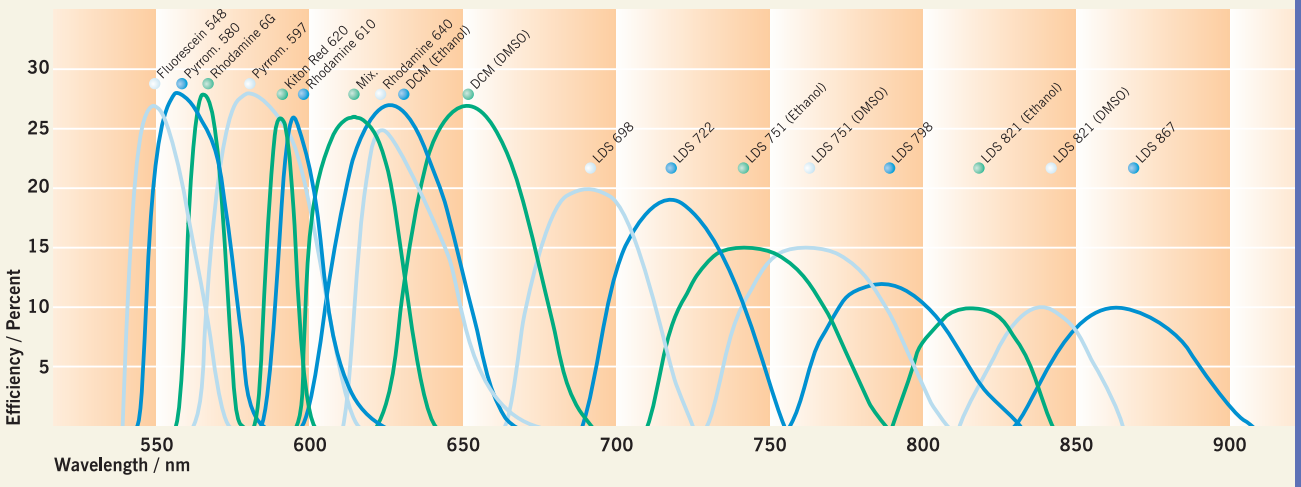

Name	Peak (nm)	Range (nm)	Efficiency	Solvent	Concentration (gram/liter)	Comment
Fluorescein 548	550	541 .. 571	27 %	Ethanol + H_2O	0.40	+ 0.2 g/l NaOH
Pyrromethene 580	557	547 .. 581	28 %	Ethanol	0.20	
Rhodamine 590	566	559 .. 576	28 %	Ethanol	0.09	Rhodamine 6G
Pyrromethene 597	582	566 .. 611	28 %	Ethanol	0.16	
Kiton Red 620	591	585 .. 600	26 %	Ethanol	0.20	Sulforhodamine B
Rhodamine 610	596	588 .. 614	26 %	Ethanol	0.20	Rhodamine B
Mix. Rh 610 / Rh 640	615	598 .. 636	26 %	Ethanol	0.17 / 0.04	
Rhodamine 640	624	614 .. 662	25 %	Ethanol	0.25	Rhodamine 101
DCM	627	602 .. 660	27 %	Ethanol	0.30	
DCM	651	626 .. 685	27 %	DMSO	0.30	
LDS 698	692	667 .. 720	20 %	Ethanol	0.25	Pyridine 1
LDS 722	718	691 .. 751	19 %	Ethanol	0.25	Pyridine 2
LDS 751	744	712 .. 782	15 %	Ethanol	0.15	Styryl 8
LDS 751	764	733 .. 802	15 %	DMSO	0.15	Styryl 8
LDS 798	785	758 .. 826	12 %	Ethanol	0.14	Styryl 11
LDS 821	815	791 .. 839	10 %	Ethanol	0.13	Stryryl 9
LDS 821	839	814 .. 862	10 %	DMSO	0.13	Styryl 9
LDS 867	863	832 .. 900	10 %	Ethanol	0.15	

Peak: Output maximum of tuning curve.

Efficiency: Laser output at the maximum of tuning range, relative to pump laser output. Efficiencies may change depending on configuration or pump power level.

Solvent: The solvent influences the peak wavelength of the dye. Methanol, ethanol, isopropanol and propylene carbonate are to a certain extend interchangeable.

Concentration: Amount of dye, in grams, for 1 liter stock solution. Higher concentrations causes a shift of tuning curves to the red, while lower concentrations may result in a blue shift. Use approximately a third of the given concentration for amplifiers. Refer to the manual for capillary cells or single cell lasers.

sirah
Laser- und Plasmatechnik

Sirah
Laser- und Plasmatechnik GmbH

An der Feuerwache 10
D-41564 Kaarst
Phone: +49 (0)2131.66 06 51
Fax: +49 (0)2131.66 80 95
http://www.sirah.com

09/2003

Acknowledgements

This work would not be possible without the people that helped me get to that point and beyond it. First and foremost, I would like to thank Dr. Katerina Chrysalidis for being truly the most dedicated, punctual and patient supervisor anyone can ask for. I feel very lucky to have been her student and I thank her for standing me and standing up for me. A very special "thank you" also goes out to Bruce for giving me many chances and to the whole RILIS team for their help, high tolerance for stupid questions and cheeky sense of humour (especially Reinhard). Everyone I worked with made my stay at CERN very special and I am beyond excited to continue working with this team.

I would also like to thank Dinko Atanasov for choosing me as a summer student in 2019 which paved the way for me to continue working at CERN and for being a great supervisor and friend.

None of my professional merits would be possible without all of the great professors at Sofia University. Special thanks to prof. Dr. habil. Georgi Rainovski for all of the support (even when I was a very annoying student).

On a personal note, thank you, Cami for giving me unrealistic expectations of the limits of a friendship. Thank you, Joos for saving me 3 months of Python struggle and being an amazing friend and late night conversationalist circa 2019. A very sincere gratitude goes out to all of my other friends at CERN - old, new and last-minute. I would genuinely like to name you all, but it does not make a good impression to have the acknowledgements be longer than the thesis. I truly could not get this far without all of you.

Благодаря на всички приятели от ФзФ, които ме бутаха смело по този път всяка сряда след лекции... Особени благодарности на Цани и на Цвети, защото без тях последните години нямаше да ги изтърпя толкова "спокойно". Благодаря на Маги, че съществува.

Благодаря на цялото си семейство - на тези, които са тук и най-вече на тези, които не са, за подкрепата и за това, че винаги са били най-големите ми фенове. Благодаря на мама и тати, че ме отгледаха отлично. Особена благодарност искам да изразя към дядо Сашо за това, че като дете не ми даваше да си получа подаръка докато не сметна корен квадратен от четирицифрено (или повече) число.

List of Figures

Bibliography

[1] Mobs, Esma, July 2019. The CERN accelerator complex - 2019. https://cds.cern.ch/record/2684277

[2] http://riliselements.web.cern.ch/

[3] https://physics.nist.gov/cgi-bin/ASD/energy1.pl?de=0&spectrum=Cd+I&submit=Retrieve+Data&units=0&format=0&output=0&page_size=15&multiplet_ordered=0&conf_out=on&term_out=on&level_out=on&unc_out=1&j_out=on&lande_out=on&perc_out=on&biblio=on&temp=

[4] K. Burns and K. B. Adams, Energy Levels and Wavelengths of Natural Cadmium and of Cadmium-114, J. Opt. Soc. Am. 46, 94–99 (1956), DOI:10.1364/JOSA.46.000094

[5] D. R. Wood and K. L. Andrew,Arc Spectrum of Lead, J. Opt. Soc. Am. 58, 818–829 (1968) DOI:10.1364/JOSA.58.000818

[6] J. Lotrian, Y. Guern, J. Cariou, and A. Johannin-Gilles, Experimentally determined transition probabilities of the systems 6p2 → 6p6d, 6p7s, 6p8s of neutral lead, J. Quant. Spectrosc. Radiat. Transfer 21, 143–146 (1979) DOI:10.1016/0022-4073(79)90025-6

[7] Tobias Kron. Konzeption, Aufbau und Testeiner Referenzzelle für die resonante Laserion-isation. Diplomathesis, Johannes Gutenberg- Universität Mainz, 2011

[8] J. Wessolek, Development of a Laser Resonance Ionization Scheme for Lead Using Titanium Sapphire Lasers for Radioactive Isotope Delivery at the TRIUMF ARIEL Facility, Technische Universität Darmstadt, July 2020

[9] http://riliselements.web.cern.ch/?element=Pb

[10] https://physics.nist.gov/cgi-bin/ASD/energy1.pl?de=0&spectrum=Cd+I&submit=Retrieve+Data&units=0&format=0&output=0&page_size=15&multiplet_ordered=0&conf_out=on&term_out=on&

level_out=on&unc_out=1&j_out=on&lande_out=on&perc_out=on&
biblio=on&temp=

[11] Arc Spectrum of Lead, D. R. Wood and K. L. Andrew, J. Opt. Soc. Am. 58, 818–829 (1968) DOI:10.1364/JOSA.58.000818

[12] L. Vazquez Rodriguez *et al.*, INTC-P-606, CERN-INTC-2021-035 (12 May 2021)

[13] Wessolek, Julius. (2020). Development of a Laser Resonance Ionization Scheme for Lead Using Titanium Sapphire Lasers for Radioactive Isotope Delivery at the TRIUMF ARIEL Facility [Zenodo]. https://doi.org/10.5281/zenodo.4298406

[14] S. A. Bhatti et al. "Three-step excitation of the 6p3/2 ns, nd, ng autoionizing Rydberg levels via the 6p6f1/2[5/2]2 level of lead". J. Phys. B: At., Mol. Opt. Phys. 30 (1997).

[15] A. Ahad et al. "Three-step laser excitation of the 6p3/2 ns, nd, ng autoionizing Rydberg levels via the 6p5f1/2[5/2]2 level of lead". Eur. Phys. J. D 32.3 (2005). DOI:10.1140/epjd/e2005-00012-2.

[16] Tobias Kron., Konzeption, Aufbau und Test Einer Referenzzelle für die resonante Laserionisation. Diploma thesis, Johannes Gutenberg-Universität Mainz, 2011.

[17] Valentin Fedosseev et al 2017 J. Phys. G: Nucl. Part. Phys. 44 084006

[18] S. Möller, A. Andresen, C. Merschjann, B. Zimmermann, M. Prinz, and M. Imlau, "Insight to UV-induced formation of laser damage on LiB3O5 optical surfaces during long-term sum-frequency generation," Opt. Express 15, 7351-7356 (2007)

[19] L. Vazquez Rodriguez *et al.*, INTC-P-606, CERN-INTC-2021-035 (12 May 2021)

[20] Bouquerel, Elian Berthier, B Lettry, J Stora, Thierry. (2009). Atomic Beam Merging and Suppression of Alkali Contaminants in Multi Body High Power Targets: Design and Test of Target and Ion Source Prototypes at ISOLDE.

[21] W. Demtroder, "Laser Spectroscopy. Basic concepts and instrumentation", Springer, Third edition

[22] V.S. Letokhov (1987). "Laser Photoionization Spectroscopy". Academic Press, Inc., 1 edition.

[23] Lyot, B (1933). "Optical apparatus with wide field using interference of polarized light". Acad. Sci. 197

[24] Harvey, Andrew Fletcher-Holmes, David. (2003). High-throughput snapshot spectral imaging in two dimensions. Proceedings of SPIE - The International Society for Optical Engineering. 10.1117/12.485557.

[25] Robert W. Boyd (2008), Nonlinear Optics (Third Edition), Academic Press, https://doi.org/10.1016/B978-0-12-369470-6.00001-0.

[26] C. Grüning, G. Huber, P. Klopp, J. Kratz, P. Kunz, G. Passler, N. Trautmann, A. Waldek and K. Wendt. Resonance ionization mass spectrometry for ultratrace analysis of plutonium with a new solid state laser system. International Journal of Mass Spectrometry 235 (2):171–178 (2004).

[27] K. Wendt, K. Blaum, C. Geppert, R. Horn, G. Passler, N. Trautmann and B. Bushaw. Laser resonance ionization for efficient and selective ionization of rare species. Nuclear Instruments and Methods in Physics Research Section B: Beam Interactions with Materials and Atoms 204:325–330 (2003).

[28] S. Rothe. An all-solid state laser system for the laser ion source RILIS and in-source laser spectroscopy of astatine at ISOLDE, CERN. Doctoral thesis, Mainz U., Inst. Kernphys. DOI:10.17181/CERN.0HNZ.7Z6X

[29] K. Chrysalidis. Improving the spectral coverage and resolution of the ISOLDE RILIS. Doctoral dissertation. Mainz, 2019.

[30] https://www.lambda.cc/product/pellin-broca-prisms-pbp/

[31] https://doi.org/10.1364/OL.44.003924

[32] https://doi.org/10.1364/OE.384630

[33] https://doi.org/10.1364/ASSL.2020.ATu2A.5

[34] http://link.springer.com/10.1007/s10751-016-1386-2

[35] https://doi.org/10.1016/j.nimb.2019.04.020

[36] https://doi.org/10.1016/S0168-583X(02)01956-0

[37] Michael G. Littman, "Single-mode pulsed tunable dye laser," Appl. Opt. 23, 4465-4468 (1984)

[38] Zapata-Nava, Oscar Rodriguez-Montero, Ponciano Iturbe-Castillo, Marcelo Treviño-Palacios, C.G. (2011). Grating cavity dual wavelength dye laser. Optics express. 19. 3483-93. 10.1364/OE.19.003483.

[39] J. Dembczyński, E. Stachowska, M. Wilson, P. Buch, and W. Ertmer, "Measurement and Interpretation of the Odd Parity Levels of Pb I" Phys. Rev. A 49, 745–754 (1994) DOI:10.1103/PhysRevA.49.745

[40] https://docs.scipy.org/doc/scipy/reference/generated/scipy.signal.find_peaks.html

[41] https://docs.scipy.org/doc/scipy/reference/generated/scipy.optimize.curve_fit.html

[42] U.Fano,C.E.Theodosiou and J.L.Dehmer, "Electron-optical properties of atomic fields". Rev.Mod.Phys.,48:4968,Jan1976. http://link.aps.org/doi/10.1103/RevModPhys.48.49,doi:10.1103/RevModPhys.48.49.

[43] S.Rothe, T.Day Goodacre, D.V.Fedorov,V.N.Fedosseev, B.A.Marsh, P.L.Molkanov, R.E.Rossel, M.D.Seliverstov, M.Veinhard and K.D.A.Wendt, "Laser ion beam production at CERN-ISOLDE:New feature - More possibilities. doi:10.2016/j.nimb.2016.02.024.